AGU ADVANCING EARTH AND SPACE SCIENCE

Water Resources Research

RESEARCH ARTICLE
10.1029/2021WR030690

Constraining Dynamic Sediment-Discharge Relationships in Cold Environments: The Sediment-Availability-Transport (SAT) Model

Ting Zhang[1], Dongfeng Li[1], Albert J. Kettner[2], Yinjun Zhou[3], and Xixi Lu[1,4]

[1]Department of Geography, National University of Singapore, Singapore, Singapore, [2]CSDMS, University of Colorado Boulder, Institute of Arctic and Alpine Research, Boulder, CO, USA, [3]Changjiang River Scientific Research Institute, Wuhan, China, [4]Inner Mongolian Key Lab of River and Lake Ecology, School of Ecology and Environment, University of Inner Mongolia, Hohhot, China

Key Points:

- Glacier-snow-permafrost melting elevates sediment availability by enlarging erodible landscapes and enhancing channel-slope connectivity
- A sediment-availability-transport (SAT)-model is developed to simulate dynamic suspended sediment concentration (SSC)-discharge relations by integrating sediment availability controlled by thermal/fluvial processes
- The SAT-model can robustly reproduce the long-term evolution, seasonality and various event-scale hysteresis of SSC for cold basins

Supporting Information:

Supporting Information may be found in the online version of this article.

Correspondence to:

T. Zhang and D. Li,
zhang_ting@u.nus.edu;
dongfeng@u.nus.edu;

Citation:

Zhang, T., Li, D., Kettner, A. J., Zhou, Y., & Lu, X. (2021). Constraining dynamic sediment-discharge relationships in cold environments: The sediment-availability-transport (SAT) model. *Water Resources Research*, *57*, e2021WR030690. https://doi.org/10.1029/2021WR030690

Received 24 JUN 2021
Accepted 8 OCT 2021

Abstract Accelerated glacier-snow-permafrost erosion due to global warming amplifies the sediment availability in cold environments and affects the time-varying suspended sediment concentration (SSC) and discharge (Q) relationship. Here, the sediment-availability-transport (SAT) model is proposed to simulate dynamic SSC-Q relationships by integrating the sediment availability coupled by thermal processes, fluvial processes and long-term storage exhaustion into a sediment rating curve ($SSC = a \times Q^b$ with a and b as fitting parameters). In the SAT-model, increased sediment sources from glacier-snow-permafrost erosion are captured by changes in basin temperature, showing an exponential amplification of SSC when basin temperature increases. Enhanced fluvial erosion by the elevated water supply from rainfall and meltwater is captured by the factor of runoff surge, which results in a linear amplification of SSC. The SAT-model is validated for the permafrost-dominated Tuotuohe basin on Tibetan Plateau utilizing multi-decadal daily SSC/Q in-situ observations (1985–2017). Results show that sediment rating curves for Tuotuohe display significant inter-annual variations. The higher parameter-b in a warmer and wetter climate confirms the increased sediment availability due to the expanded erodible landscapes and gullying-enhanced connectivity between channels and slopes. Through capturing such time-varying sediment availability, the SAT-model can robustly reproduce the long-term evolution, seasonality, and various event-scale hysteresis of SSC, including clockwise, counter-clockwise, figure-eight, counter-figure-eight, and more complex hysteresis loops. Overall, the SAT-model can explain over 75% of long-term SSC variance with stable performance under hydroclimate abrupt changes, outperforming the conventional and static sediment rating curve approach by 20%. The SAT-model not only advances understanding of sediment transport mechanisms by integrating thermal- and fluvial-erosion processes, but also provides a model framework to simulate and project future sediment loads in other cold basins.

1. Introduction

Ongoing climate change has already significantly impacted suspended sediment loads in cold environments by regulating the sediment generation, delivery, and deposition processes (Bendixen et al., 2017; Jaeger & Koppes, 2016; Knight & Harrison, 2012; Li et al., 2021b). Substantial increases in sediment fluxes have been reported for many cold basins due to the accelerating melt of cryosphere in a warming climate (Delaney & Adhikari, 2020; Lewkowicz & Way, 2019; Li, Li, Zhou, & Lu, 2020; Overeem et al., 2017). Increased sediment fluxes threaten downstream dams and reservoirs (Nie et al., 2021; Vörösmarty et al., 2003), and impair freshwater quality and aquatic ecosystems (Best, 2019; Mather & Johnson, 2014). For small to medium sized catchments, suspended sediment transport is characterized by high temporal variability (Ahn et al., 2017; Vercruysse et al., 2017). For those, most of the annual sediment load is contributed by several high-magnitude low-frequency flood events (e.g., rainstorms and snow-ice melt events) associated with complex short-term dynamics that could cause severe socio-ecological-economic impacts (Lloyd et al., 2016; Mather & Johnson, 2014). Thus, a better understanding of the long-term evolution of suspended sediments and the short-term dynamics of extreme sediment events by for example, modeling is imperative to mitigate their downstream impacts and improve watershed management in a warming future.

Modeling of suspended sediment remains challenging because of the complex transport processes and changes in sediment availability. Sediment rating curves are commonly applied to estimate fluvial sediment

flux (Darby et al., 2016; Hilton et al., 2008; Ranasinghe et al., 2019), which are represented by a power function between suspended sediment concentration (SSC) and discharge (Q): $SSC = a \times Q^b$, with a and b as fitting parameters (Asselman, 2000; Syvitski et al., 2000). Although these rating curves reflect the overall fluvial transport pattern, such homogenous SSC-Q relations do not specifically capture the sediment availability regulated by seasonal processes such as, ever-evolving soil erodibility, erosivity of eroding agents, temporary sediment storage and release in river channels, and hydrological connectivity (Morehead et al., 2003; Pietroń et al., 2015). Although a long-term average sediment load might be captured by SSC-Q rating curves, they tend to fail to capture the widespread SSC-Q hysteretic patterns (Lefrançois et al., 2007; Walling & Webb, 1982). Especially, asynchronous peaks of SSC-Q and different SSCs in the rising and falling limbs of a hydrograph during a flood are widely observed in the real-world (Duvert et al., 2010; Li et al., 2021a; Lloyd et al., 2016; Williams, 1989). Recent studies have suggested to use an improved rating curve to reflect the hysteresis effect by considering the factors of sediment washout, slope of the hydrograph, precipitation, and antecedent hydrologic conditions (Ahn & Steinschneider, 2018; Eder et al., 2010; Mather & Johnson, 2014). Yet, most of these hysteresis models can only be fitted to a single-event scale, failing to capture the long-term sediment evolution (Eder et al., 2010; Mather & Johnson, 2014). Moreover, these improvements mainly emphasize the sediment availability amplified by pluvial processes (e.g., rainstorms; Ahn & Steinschneider, 2018; Mather & Johnson, 2014), but overlook the thermally erosional processes (e.g., new available sediments released from the melted glacier-snow-permafrost).

The sensitive response of sediment availability to thermal processes in cold environments makes it more challenging to model the suspended sediment transport and therefore aforementioned models are unsuitable here. Mounting evidence have indicated the critical control of basin temperature on sediment generation and delivery by altering landscapes and hydrological connectivity (Costa et al., 2018; Kettner & Syvitski, 2008; Li et al., 2021a; Syvitski & Milliman, 2007). With rising temperatures, the increased snowmelt erosion, thaw slumps, thermally controlled gullies, glacier erosion and accessibility to subglacial/proglacial sediment storage have become non-negligible sediment sources for many of the cold basins in (sub)Arctic and alpine regions (Delaney & Adhikari, 2020; Lewkowicz & Way, 2019; Li et al., 2021a). Besides gullies, water tracks incised by melt flow enhance the hydrological connectivity and accelerate the sediment response to disturbances (Lafrenière & Lamoureux, 2019; Rowland et al., 2010). These thermally erosional processes further magnify the SSC-Q hysteresis effect and add complexity to the hysteretic patterns (Misset et al., 2019). For instance, snow-glacier erosion or thaw slumps after the streamflow peaks can create anticlockwise or more complex hysteresis loops (Morehead et al., 2003). The accelerated atmospheric warming in cold environments necessitates the integration of temperature-controlled sediment availability into fluvial sediment transport models (Hirschberg et al., 2021; Lewkowicz & Way, 2019).

Daily in-situ observations of SSC and Q over three decades in a pristine permafrost-dominated basin (Tuotuohe basin) situated in the Tibetan Plateau provide a unique opportunity to investigate the response of dynamic SSC-Q relationships to sediment availability across various time scales. This study proposes a new model for cold environments, the sediment-availability-transport (SAT) model, that can (a) simulate long-term suspended sediment transport and dynamic SSC-Q relationships; (b) capture the time-varying sediment availability governed by the coupled thermal and fluvial processes; and (c) reproduce the seasonal- and event-scale sediment hysteresis patterns. The SAT-model advances the understanding of the thermal/fluvial controls on sediment availability and suspended sediment dynamics and provides insights on future changes of sediment loads in cold environments under a warming climate.

2. Study Site and Materials

2.1. Study Site

The SAT-model is applied in the Tuotuohe basin (headwater of Yangtze River) on the Tibetan Plateau. It has a basin area of 18,216 km^2, a river length of 350 km and an average elevation of 4,950 m a.s.l. (Figure 1a). Tuotuohe is a typical cold basin originating from the Jianggendiru Glacier which is situated on the northwestern Geladandong Peak (Figure 1b). Specifically, Tuotuohe is dominated by ice-rich permafrost (~98% of its area; Figure S11 in Supporting Information S1) and contains 92 glaciers covering an area of 389 km^2 that consists of a volume of 42 km^3 at elevations above 5,500 m a.s.l. (Li, Li, Zhou, & Lu, 2020; Wu et al., 2013). Based on isotope methods, the supra-permafrost groundwater and snow-glacier meltwater

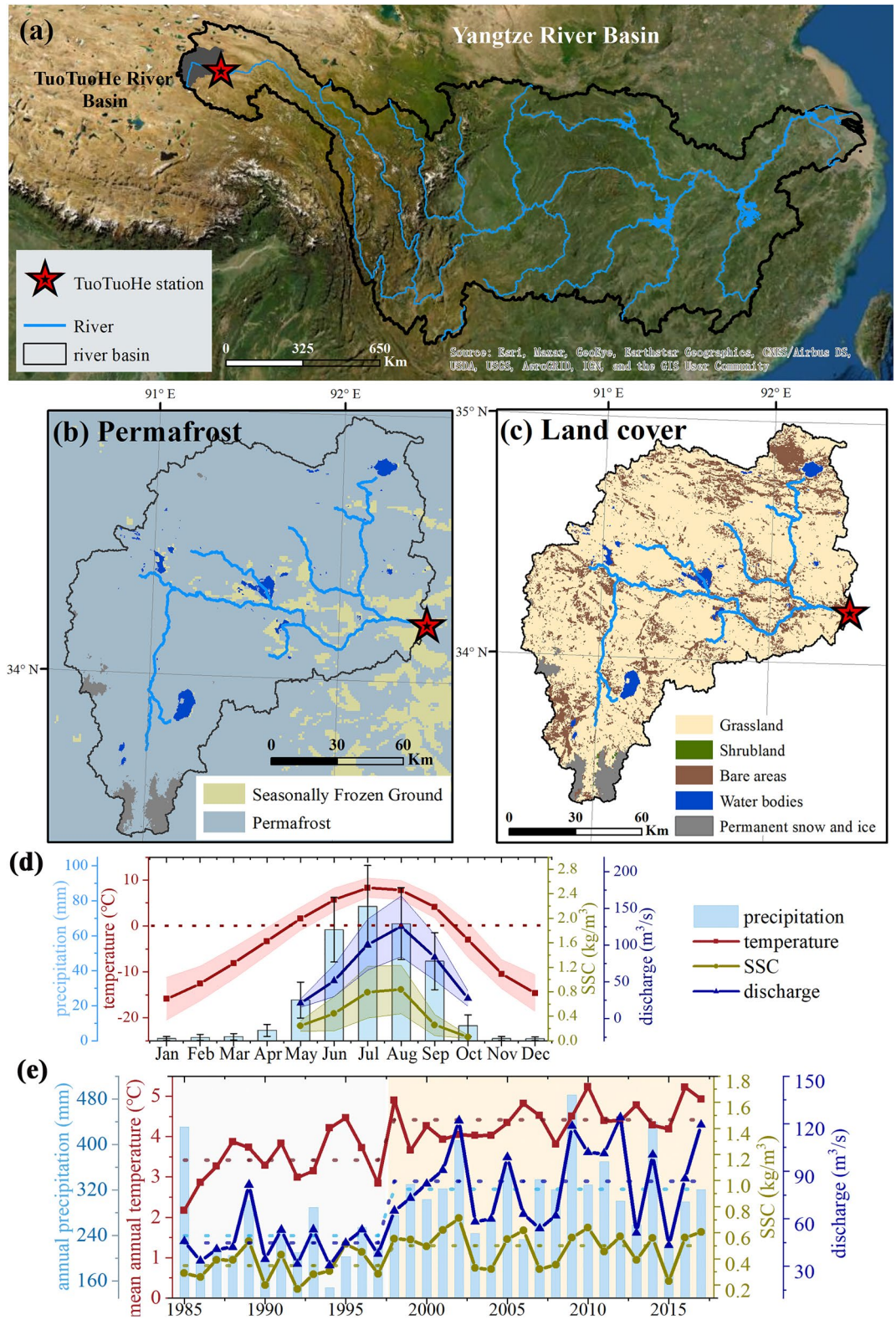

Figure 1. Climate, land cover, discharge, and fluvial sediment for the Tuotuohe river basin. (a) The location of Tuotuohe basin; (b) The distribution of permafrost; (c) The distribution of landcover types; (d) Monthly variations in temperature, precipitation, suspended sediment concentration (SSC) and discharge; (e) Trends of mean annual hydroclimate factors from 1985 to 2017.

Table 1
Different Suspended Sediment Models Used in This Study

Model	Model equation	Factors considered in the model
M_{RC}	$SSC_i = a \times Q_i^b$	Fluvial transport capacity
M_T	$SSC_i = A_i \times a_1 \times Q_i^{a_2 \times T_i + b_1}$	Thermal processes, storage exhaustion
M_F	$SSC_i = A_i \times (a_1 \times QI_i + b_1) \times Q_i^{b_2}$	Fluvial processes, storage exhaustion
M_{TF}	$SSC_i = a_1 \times Q_i^{a_2 \times T_i + b_2} + (a_3 \times QI_i + b_3) \times Q_i^{b_1} + a_4 \times Q_i$	Thermal and fluvial processes
M_{SAT}	$SSC_i = A_i \times a_1 \times Q_i^{a_2 \times T_i + b_2} + A_i \times (a_3 \times QI_i + b_3) \times Q_i^{b_1} + a_4 \times Q_i$	Thermal and fluvial processes, storage exhaustion

Note. The suspended sediment concentration SSC_i (kg/m^3) for a given day i can be estimated by a specific model defined in Table 1, where Q_i is the daily discharge (m^3/s); A_i is a dimensionless geomorphic exhaustion index; T_i is the 8-day average temperature (°C); QI_i is the 2-day discharge increase (m^3/s) and a_n and b_n are the fitting parameters.

contribute 51% and 23% to the total runoff respectively (Zong-Jie et al., 2018). Geologically, Tuotuohe consists of quaternary fluvial deposits, Mesozoic clastic rocks, carbonates, evaporites, and volcanic rocks, with soils dominated by Gelic Leptosols (Li, Li, Feng, et al., 2020). Basin sediments are generated and delivered by channel erosion, snowmelt erosion, glacier erosion, thaw slumps and thermo-erosion gully induced by permafrost degradation, and mass wasting triggered by rainstorms. The main landcover comprises grassland (high-cold meadow and steppe) and bare ground (Figure 1c), with negligible human impacts. Thus, Tuotuohe is an ideal basin to investigate the response of sediment transport to natural processes and for validating our SAT-model.

Climatically, Tuotuohe is affected by the Indian monsoon and Westerlies, in an alpine climate setting (Du et al., 2019). The mean annual temperature and mean total annual precipitation are −3.4°C and 298 mm respectively, and the basin experiences a melting season from May to September. Ninety-five percent of the annual precipitation falls between May and October (Figure 1d), when over 90% of precipitation is contributed by rainfall (Li et al., 2021a). Specifically, snowmelt mainly occurs in spring (May–June) and autumn (e.g., September), with two peaks in June and September (Wang et al., 2015). The glaciers and frozen ground melt in summer (July–August; Wu et al., 2013). Over the past decades, the Tuotuohe region experienced an apparently warming and wetting climate (Li, Li, Zhou, & Lu, 2020), with increases of annual mean temperature and precipitation by 1.4°C and 30% (40 mm), respectively, after 1997 (Figure 1e). Accordingly, the glacier areas in the Geladandong region decreased by 5% and the active layer thickness of permafrost was estimated to be increased over 40 cm (Shi et al., 2020; Yao et al., 2014), associated with substantially elevated runoff (+78%) and sediment loads (+135%) after 1997 (Li, Li, Zhou, & Lu, 2020).

2.2. Materials

Daily meteorological (temperature and precipitation) and hydrological (discharge and suspended sediment concentration) observations from 1985 to 2017 were collected from Tuotuohe station (92.47°E, 34.22°N). Meteorological observations are from January to December, whereas hydrological variables are only observed during the melting season (May to October). Daily discharge (Q, m^3/s) is measured utilizing the current meter and an Acoustic Doppler Current Profiler (ADCP). Daily suspended sediment concentrations (SSC, kg/m^3) are sampled by depth-integrating samplers. Normally, hydrological variables are observed once a day, while they are observed more frequently (e.g., four times a day) during flood events to capture more likely high sub-daily variations. Detailed strategies and potential uncertainties of discharge and SSC measurements in the Tuotuohe station can be found in Li et al. (2021a).

Snow coverage (%) in Tuotuohe from 2000 to 2015 was derived from MODIS/Terra Snow Cover Daily L3 Global data set at 500 m spatial resolution (https://nsidc.org/data/MOD10A1/versions/6).

Earlier studies suggest that Tuotuohe hydroclimate experienced an abrupt change in 1997 (Li, Li, Zhou, & Lu, 2020). Therefore, the observations from 1998 to 2017 are used to develop the SAT-model and to compare the model performance with other models (Table 1). The observations from the entire period (1985–2017) are then used to conduct a cross-validation to evaluate the robustness of the SAT-model.

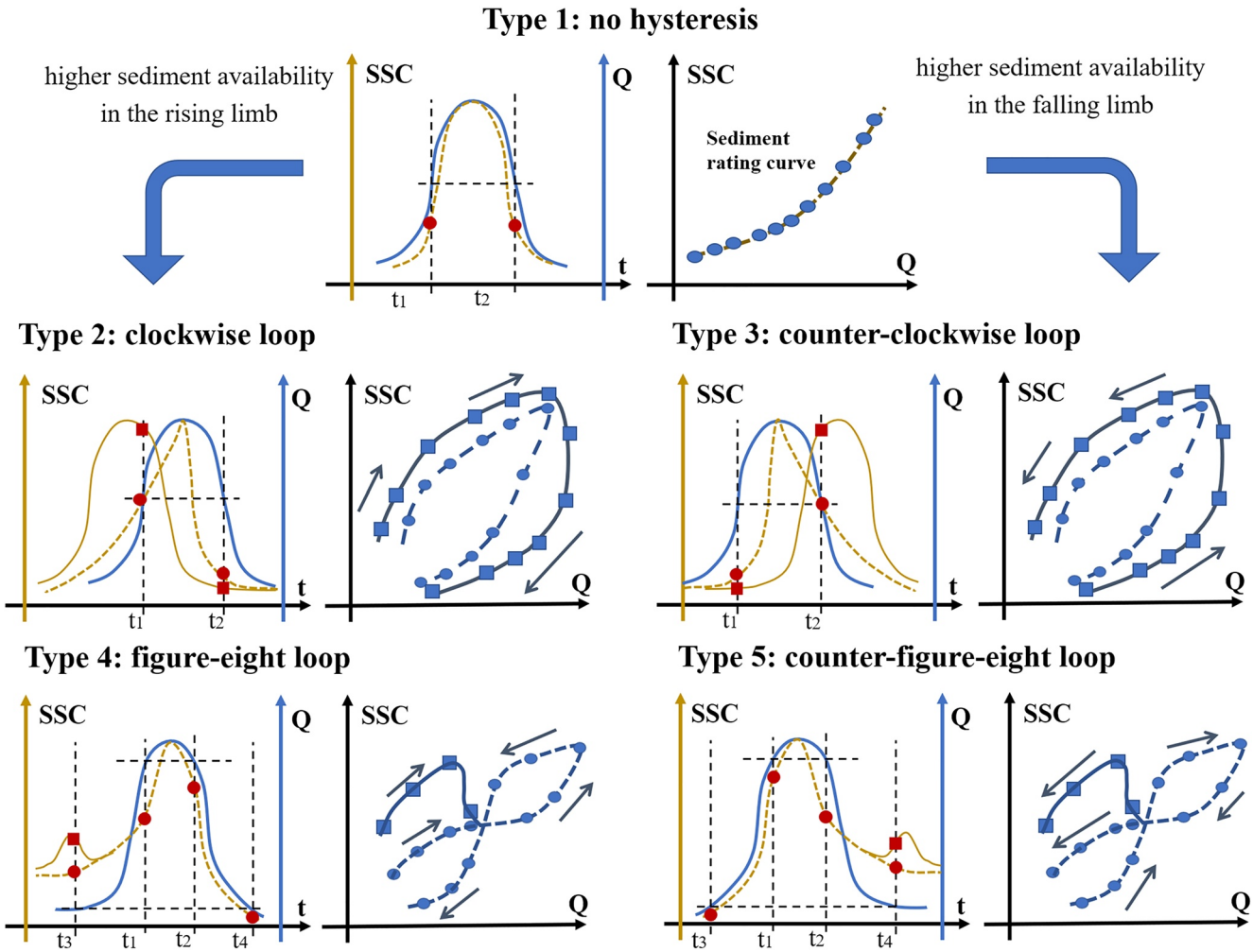

Figure 2. Schematic illustration of five types of suspended sediment concentration (SSC)-discharge (Q) relationship at an event scale, updated from Williams (1989). For each type, changes in SSC and Q over time are presented in the left panel and the corresponding hysteresis loop is provided in the right panel. In the left panel, the brown solid line represents the SSC peaking asynchronously with Q; the brown dotted line represents the SSC peaking synchronously with Q; blue line represents Q. The red circles and squares denote the SSC at the same discharge. In the right panel, squares denote SSC-Q relationship when SSC and Q peak asynchronously, and circles denote that SSC-Q relationship with synchronous peak.

3. Methods

3.1. Sediment-Discharge Hysteresis

Sediment hysteresis loops describe the evolution of SSC-Q relationship over time and provide a tool to isolate the response of SSC to sediment availability (Williams, 1989). When SSC is only constrained by transport capacity (Q) with unlimited sediment supply, there is no hysteresis effect (Smith & Dragovich, 2009); so for such conditions, applying a sediment rating curve would be sufficient to estimate the sediment dynamics (Type 1 in Figure 2). Hysteresis is caused by time-varying sediment supply and storage (Pietroń et al., 2015). For cold environments, highly variable sediment availability due to thermal erosion, seasonal meltwater erosion and sporadic rainfall erosion creates various shapes of hysteresis loops (Duvert et al., 2010; Misset et al., 2019), and four types will be discussed here (Figure 2).

A clockwise hysteresis loop (Type 2) describes an earlier SSC peak or coincident peaks with higher SSC in the rising limb. It can be interpreted as the high reliance of sediment supply on proximal and readily available sources (e.g., in-channel storage, gullies, bank erosion, and slumps), but these sources become exhausted during the falling limb (Juez et al., 2018; Li et al., 2021a). A counterclockwise hysteresis loop (Type 3) can be induced by, for example, late arrival of sediments from relative remote sources, delayed input of

in-channel deposits, or due to sediment replenishment in the falling limb (e.g., flushing floodplains during flow recession, the emergence of meltwater, and bank collapse in the falling limb; Juez et al., 2018; Langlois et al., 2005).

A figure-eight hysteresis loop (Type 4) includes a clockwise loop during low discharges and a counter-clockwise loop during high discharges. Figure-eight loops form during transient proximal sediment supply at the beginning and insufficient sediment supply as discharge rises rapidly and more sediment supply after the peak discharge, followed by a sediment exhaustion phase when discharges decrease again (Lloyd et al., 2016). A counter-figure-eight hysteresis loop (Type 5) occurs when there is limited sediment supply in the very beginning of the rising and falling limbs, but then elevated levels of sediment availability follow due to late sediment replenishment (Smith & Dragovich, 2009).

3.2. Sediment-Availability-Transport (SAT) Model

Suspended sediment transport is controlled by both fluvial transport capacity and sediment availability (Mather & Johnson, 2014; Walling & Webb, 1982). Fluvial transport capacity is usually expressed in terms of discharge (Q), whereas parameterization of the sediment availability is rarely considered in earlier studies (e.g., Ahn et al., 2017; Pietroń et al., 2015). Here, a sediment-availability-transport (SAT) model (M_{SAT} in Table 1) is developed to simulate SSC by integrating the sediment availability coupled with thermal processes, fluvial processes and long-term storage exhaustion and expressed by modifying a traditional rating curve (M_{RC} in Table 1).

First, in cold environments, sediment generation is sensitive to basin temperature due to thermally controlled sediment sources (e.g., thaw slumps, thermal gullies, and thermal bank erosion). An increase in sediment sources is defined by the b-coefficient in M_{RC} (Table 1 and Figure 3b), where a larger b indicates a higher sediment availability (Asselman, 2000; Syvitski et al., 2000). This exponential magnification of SSC driven by temperature will be further justified in Section 4.2. Additionally, there will be time lags in the response of the measured SSC to these thermal processes because of the long-distance travel for the upstream sediment from glaciers/slopes to the basin outlet and energy consumed for glacier/permafrost melting (Bolch et al., 2019; Misset et al., 2019). A 1-week antecedent temperature is selected to reflect the delayed response (exploring the impacts of different time-lags is discussed in Supporting Information S1). The thermally controlled sediment transport in the SAT-model is expressed as a function of the 8-day average temperature (T):

$$\mathrm{ssc}_i = a_1 \times Q_i^{a_2 \times T_i + b_1}, \text{ with } \quad T_i = \sum_{k=i-7}^{i} \left(t_k/8\right), \tag{1}$$

where, for a given day i, ssc_i is the estimated suspended sediment concentration (kg/m^3); Q_i is the discharge (m^3/s); T_i is the 8-day average temperature; t_i is the daily average temperature (°C) and a_n and b_n are the fitting parameters.

Second, sediment availability is also enhanced by increased glacier-snow meltwater and rainfall induced flows. The rising seasonal meltwater can not only enhance the erosive power, but also boost channelization by gullying (Lafrenière & Lamoureux, 2019). The runoff surge during rainstorms can trigger debris flows that carry bulks of sediments downstream (Simoni et al., 2020). In the SAT-model, the intensified erosion that coincide with a runoff surge is defined as a function of a 2-day discharge increase (QI in Equation 2; the comparison of different QI is discussed in Supporting Information S1). Such enhanced erosivity due to a runoff surge is found to be relevant to the a-coefficient in M_{RC} (Table 1), representing sediment flushing in the rising limb (Asselman, 2000; Mather & Johnson, 2014). The linear magnification induced by the runoff surge to SSC will be further justified in Section 4.2.

$$\mathrm{ssc}_i = \left(a \times \mathrm{QI}_i + b_1\right) \times Q_i^{b_2}, \text{with } \mathrm{QI}_i = \begin{cases} Q_i - Q_{i-1} & \text{if } Q_i > Q_{i-1} \\ 0 & \text{else} \end{cases} \tag{2}$$

where, QI_i represents a 2-day discharge increase (m^3/s) for a given day i, and a_n and b_n are fitting parameters.

The third term ($a_4 \times Q$) in the SAT-model (Table 1) represents sediment transport that is less impacted by previous storage and changes of temperature and discharge. This erosion process is more apparent during the low-flow period (e.g., channel erosion by baseflow for October in Tuotuohe) when temperature and

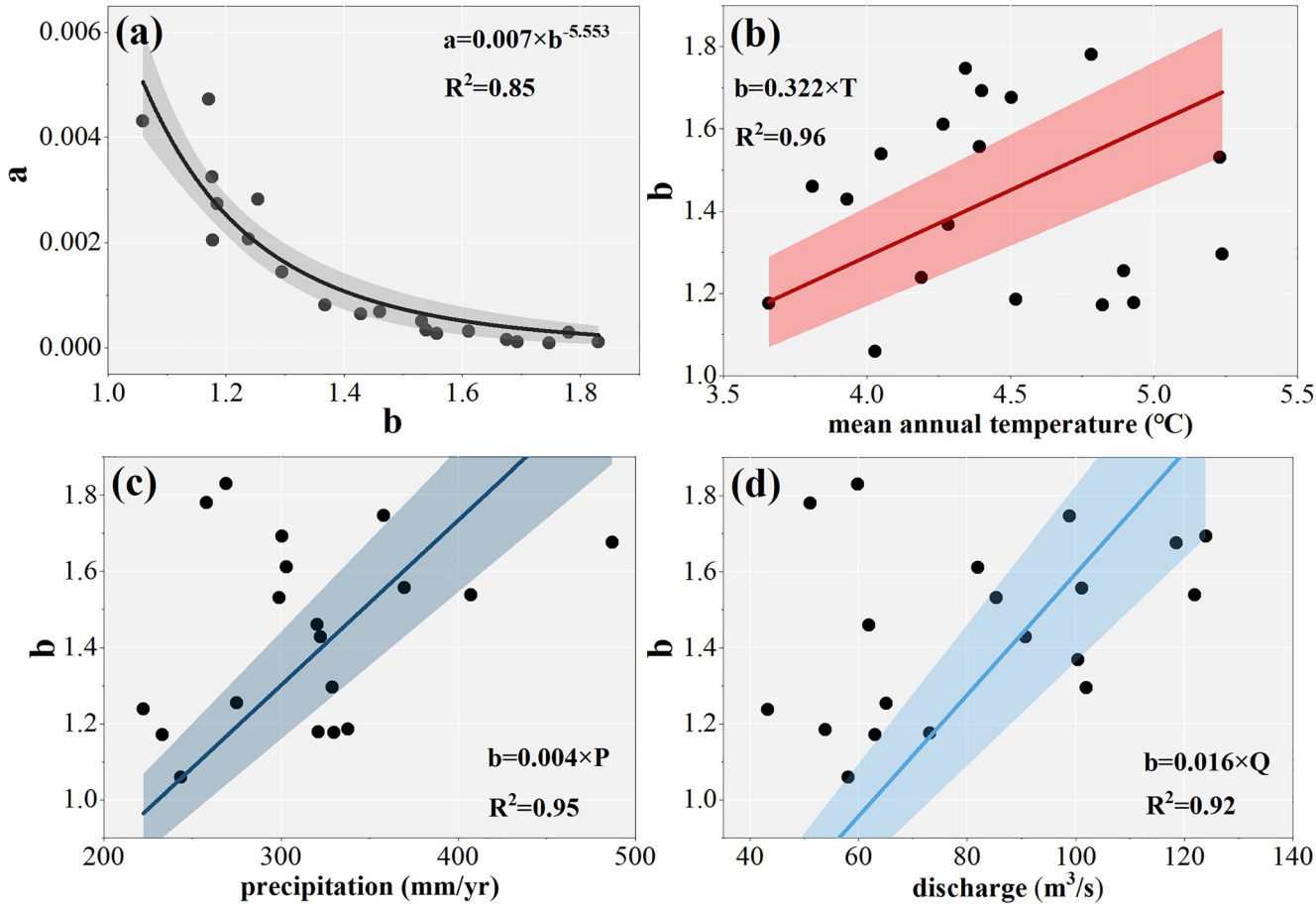

Figure 3. Inter-annual variation in rating curve parameters (function M_{RC}, Table 1) under a warming and wetting climate for Tuotuohe river basin during 1998-2017. (a) Power-law relationship between *a* and *b*. (b) Linear relationship between *b* and mean annual temperature (*T*). (c) Linear relationship between *b* and annual precipitation (*P*). (d) Linear relationship between *b* and annual discharge (*Q*). All the linear trendlines in panels (b, c and d) are fitted by fixating the *y*-intercept at zero, thus R^2 in Figures 3b, 3c and 3d are incomparable with that in Figure 3a. The shaded areas denote the 95% confidence intervals of the corresponding fitting lines. Notably, the *b*-coefficient of the annual sediment rating curve is impacted by multiple hydroclimatic factors simultaneously and varies substantially from year to year, resulting in its poor correlation with a single factor. Here, the intercept is fixed at 0 to capture the impacts of the potential amplification effect of each single hydro-climatic variable on *b*-coefficient.

runoff surge are relatively low and the aforementioned thermally/pluvially enhanced erosion processes are weak. Moreover, a linear magnification induced by the discharge (or baseflow) to SSC has been observed during October in Tuotuohe (Figure S1b in Supporting Information S1).

Furthermore, the long-term depletion of sediment storage from previous years is integrated into the SAT-model to modify the enhanced sediment availability with rising temperatures and runoff surge. Inspired by the "washout" process proposed by VanSickle and Beschta (1983), the previous sediment storage is assumed to be continuously depleted throughout a hydrological year, causing a low sediment supply. In the SAT-model, this storage exhaustion (e.g., geomorphic exhaustion index) is defined as a function of discharge (Equation 3) and is rescaled as a fraction between 0 and 1, by a Sigmoid function. An illustration of changes in the geomorphic exhaustion index within a hydrological year is provided in Figure S2 in Supporting Information S1.

$$A_i = \frac{\sum_{j=1}^{TD} Q_j}{\sum_{j=1}^{i} Q_i}; \text{Sigmoid}\left(A_i\right) = \frac{1}{1+e^{-A_i}} \quad (3)$$

where, A_i is the dimensionless geomorphic exhaustion index for a given day, calculated as the total annual runoff for a given year divided by the cumulative runoff by day *i*. TD is the number of days within a hydrological year.

In the following, the five models in Table 1 will be evaluated by analyzing the long-term SSC simulations and the SSC-*Q* hysteresis at an event-scale.

3.3. Model Fitting and Evaluation

The listed models (Table 1) are fit by nonlinear least squares curve fitting using the Levenberg-Marquardt (L-M) algorithm. This algorithm combines the Gauss-Newton method and the steepest descent method, and is robust for most cases (Gan et al., 2018).

To further demonstrate the model robustness, the SAT-model and the M_{RC} sediment rating curve in Table 1 are tested by ten-time cross-validation using the entire available data set during 1985–2017. Notably, in each cross-validation, the calibration period is the randomly selected 10 years during 1985–2017. The validation period is the remaining 23 years from 1985 to 2017.

Model performance is evaluated by Nash-Sutcliffe efficiency coefficient (NSE, $-\infty$ to 1; Nash & Sutcliffe, 1970), Coefficient of determination (R^2, 0–1) and the Relative error (RE). RE is defined as the sum of difference between simulated and observed SSC divided by the sum of SSC observations. A model with NSE and R^2 over 0.5 and RE less than 25% can be considered an accurate model (Ara Rahman & Chakrabarty, 2020; Mather & Johnson, 2014).

Finally, the events with SSC peaks over 2.9 kg/m^3 (the top 1 percentile) from 1998 to 2017 are also selected to validate the model's performance in simulating extreme SSC events. The beginning of the event is defined as the first day of a rising limb and the end of the event is defined as the last day of a falling limb. The consecutive extreme peaks are considered as a single event. According to the maxima SSC in each event, the top-10 extreme sediment events are selected for comparison.

4. Results

4.1. Temporal Variation in SSC-*Q* Relationships

The sediment rating curve (M_{RC} in Table 1) is fitted for each year independently during 1998–2017 to investigate dynamic SSC-*Q* relationships at an inter-annual scale. For the Tuotuohe basin, SSC-*Q* relationships vary significantly (Figure 3a and Table S1 in Supporting Information S1). Specifically, the temporal variations in rating parameters (a and b) indicate the significant inter-annual changes of SSC under the same discharge, with b ranging from 1.06 to 1.83. Meanwhile, there is a strong inverse correlation between a and b and 85% of the variation of a can be explained by b ($R^2 = 0.85$, Figure 3a). Moreover, the time-varying sediment transport can be influenced by the warming and wetting climate over the past decades (Figures 3b–3d). For instance, there is a general upward trend of b with mean annual temperature (Figure 3b). The increased annual precipitation and runoff can also lead to the increase of b (Figure 3d), respectively. The elevated parameter-b during the warming and wetting climate indicates more pronounced sediment transport during high flows and more extreme sediment events.

Apart from the inter-annual variation, SSC-*Q* relationships also display apparent seasonal variations. Specifically, SSC can vary over two orders of magnitude under the same discharge (Figure 4a). From the monthly averaged SSC-*Q* relationships, a clockwise loop can be observed, with high SSCs in summer (0.95 kg/m^3) and low SSCs in autumn (0.18 kg/m^3; Figure 4a). However, the sediment rating curve M_{RC} fails to reproduce this seasonal hysteretic pattern and can only explain 54% of the SSC variance (Table 2), associated with significant scatters around the regression line. But, the hysteresis described above can be reflected by the 8-day average temperature, 2-day discharge increase and the daily precipitation (Figure 4b and Figure S3 in Supporting Information S1). For similar discharges, these hydroclimate variables (e.g., temperature, runoff surge, and precipitation) are higher in spring and summer than in autumn.

4.2. Sediment Availability Amplified by Rising Temperature and Runoff Surge

For cold basins like Tuotuohe, sediment availability can be impacted by the basin temperature and runoff surge; both are significantly correlated with SSC (Figure 5). Specifically, SSC exponentially increases with the basin temperature and 35% of the SSC variance can be explained by the 8-day average temperature (with

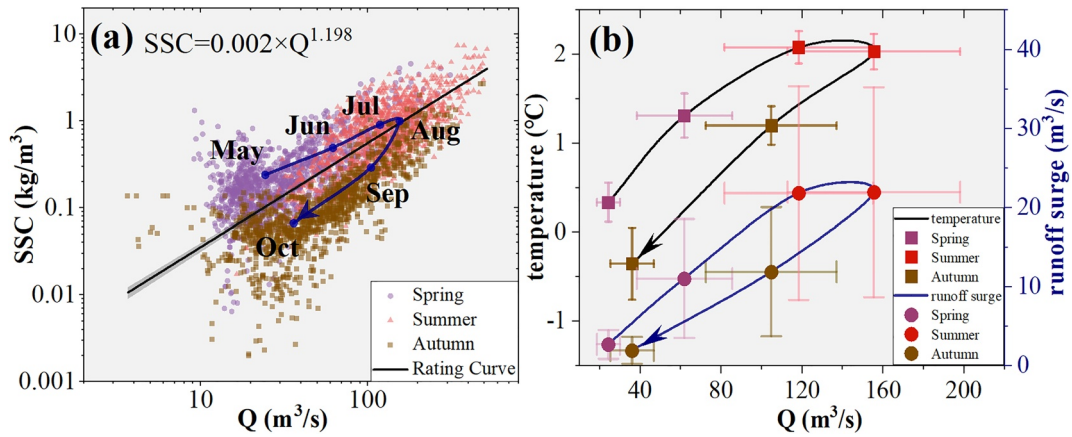

Figure 4. Hysteresis in suspended sediment concentration (SSC)-discharge (Q) relationship and hydroclimate variables—discharge relationships. (a) Daily SSC-Q relationship. The blue dots represent the monthly average values. The black line corresponds to the overall sediment rating curve fitted by daily SSC-Q observations during 1998–2017. The shading area indicates 95% confidence interval. (b) Monthly average hydroclimate variables—discharge relationships from May to October. Temperature for a particular month is the mean of the 8-day average temperatures. Runoff surge for a particular month is the mean of the 2-day discharge increase. For more detailed calculations, see Section 2.2 in Method. Error bars denote the standard deviations.

1-week antecedence, T; Figure 5a). This exponential relation between the temperature and SSC is stronger at the monthly scale, with $R^2 = 0.89$ (Figure 5b). Despite the significant positive correlation, extreme SSCs (e.g., the top 1 percentile with SSC over 2.9 kg/m^3) are not coinciding with the warmest conditions (e.g., the top 1 percentile with T over 3°C), but occur during relatively warm conditions (T ranging from 1°C to 3°C; Figure 5a and Figure S4 in Supporting Information S1). At the monthly scale, the SSC peaks in August instead of July, when the temperature peaks (Figure 5b). The lower SSC in extreme warm conditions can be induced by less precipitation and weaker runoff surge (Figures S4c and S4d in Supporting Information S1). Such impact of extreme warm conditions on sediment availability can be captured by the runoff surge in the SAT-model.

Compared with temperature, a more significant linear correlation is found between SSC and runoff surge, which explains 69% of the variance of SSC (Figure 5c). An even more apparent linear relationship is found at a monthly scale ($R^2 = 0.86$; Figure 5d). Importantly, extreme SSCs are more likely governed by the surge of discharge. For example, there is a greater response of SSC to runoff surge and a steeper slope when SSC exceeds 2.9 kg/m^3, with coincident peaks of SSC (7.43 kg/m^3) and runoff surge (211 m^3/s; Figure 5c).

Compared to the runoff surge, precipitation is a poor indicator of SSC temporal variation; less than 40% of SSC variation can be explained by precipitation (Figure S5 in Supporting Information S1). Although SSC

Table 2
An Overall Comparison of Model Performance and Model Function

Model	NSE	RE (%)	R^2	Model function
M_{RC}	0.54	−3.3	0.54	$SSC_i = 0.002 \times Q_i^{1.198}$
M_T	0.68	−5.5	0.68	$SSC_i = A_i \times 0.004 \times Q_i^{0.0.75 \times T_i + 1.011}$
M_F	0.70	−0.4	0.71	$SSC_i = A_i \times (0.0006 \times QI_i + 0.008) \times Q_i^{1.006}$
M_{TF}	0.75	0.0	0.75	$SSC_i = 0.006 \times Q_i^{0.180 \times T_i + 0.568} + (0.017 \times QI_i + 0.057) \times Q_i^{4E-14} + 0.0005 \times Q_i$
M_{SAT}	0.77	1.5	0.77	$SSC_i = A_i \times 0.002 \times Q_i^{0.211 \times T_i + 0.670} + A_i \times (0.099 \times QI_i + 0.059) \times Q_i^{0.133} + 0.002 \times Q_i$

Note. The suspended sediment concentration SSC_i (kg/m^3) for a given day i can be estimated by a specific model defined in Table 1, where Q_i is the daily discharge (m^3/s); A_i is a dimensionless geomorphic exhaustion index; T_i is the 8-day average temperature (°C); and QI_i is the 2-day discharge increase (m^3/s). NSE stands for Nash-Sutcliffe efficiency coefficient, RE stands for Relative Error and R^2 is the coefficient of determination.

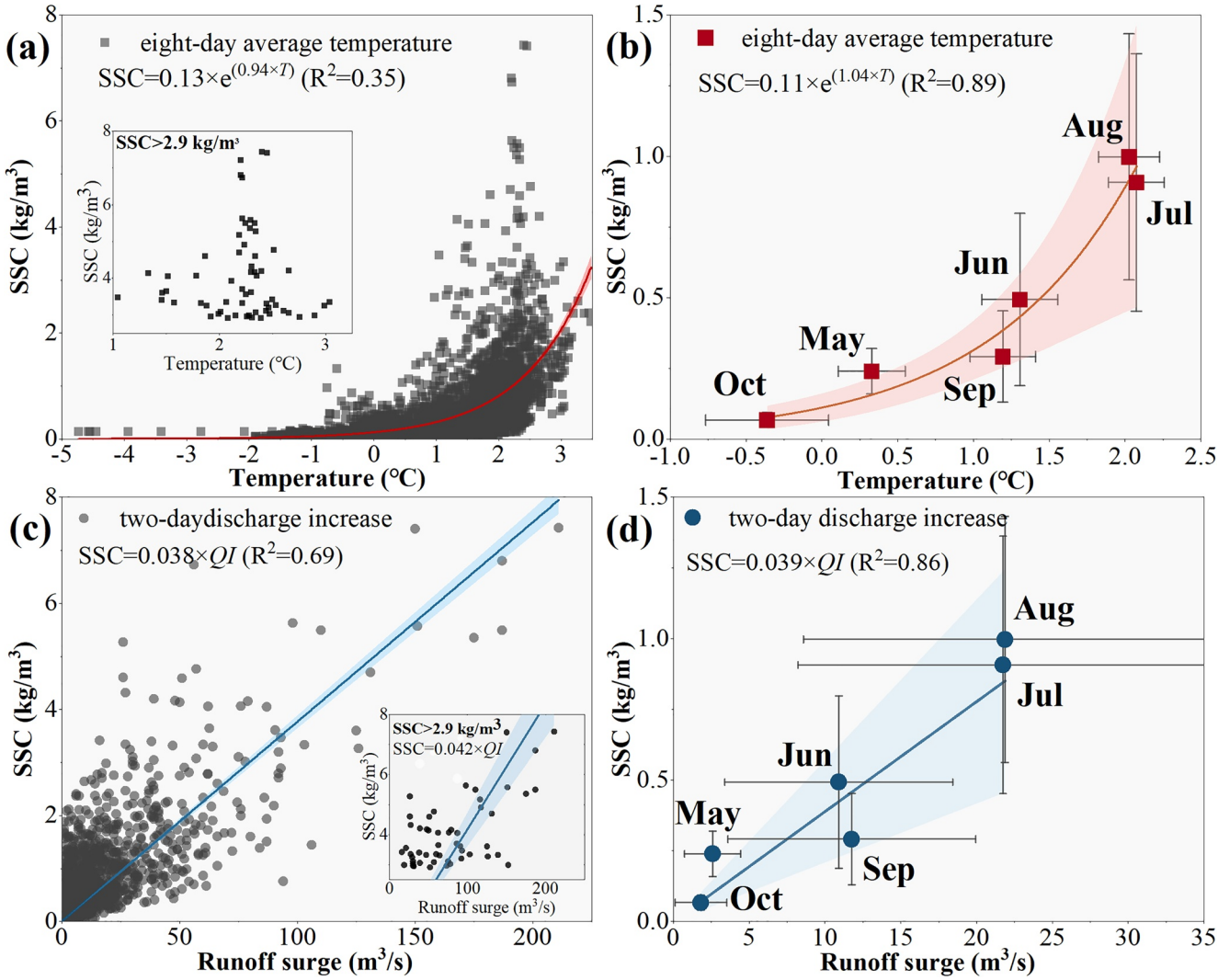

Figure 5. Relation between suspended sediment concentration (SSC), 8-day average temperature (*T*) and 2-day discharge increase (QI) at daily and monthly scales for 1998–2017. (a) Daily SSC-*T* relationships. (b) Monthly SSC-*T* relationship. (c) Daily SSC-QI relationships. (d) Monthly SSC-QI relationship. For more detailed calculations of *T* and QI, see Section 3.2. The shaded areas denote the 95% confidence intervals of the corresponding fitting lines.

exhibits an increasing trend with precipitation ($R^2 = 0.28$), the extreme sediment values are mainly observed during medium precipitation with daily precipitation ranging from 5 to 15 mm (Figure S5a in Supporting Information S1). To include the antecedent precipitation and the time-lag of response, the correlation between 2-day average precipitation and SSC is also investigated, but only a limited improvement is found ($R^2 = 0.38$; Figure S5c in Supporting Information S1). In Tuotuohe station, the precipitation during the melt season is dominated by rainfall (over 90%; Li et al., 2021a). The impact of precipitation on sediment transport can be complicated by the inconsistent time-lags of sediment response during or right after different rainfall intensities and the spatial heterogeneousness of rainfall events. Thus, precipitation is not directly accounted for in the SAT model.

4.3. Simulation of a Dynamic SSC-*Q* Relationship by the SAT-Model

The SAT-model unequivocally performs best for the Tuotuohe basin compared to other models (Table 2). Specifically, the SAT-model can account for 77% of the daily SSC variance, which is much better than the 54% explained by the M_{RC} sediment rating curve (Table 2). Pearson's correlation coefficient (*R*) between estimated and observed SSC can reach 0.88 for the SAT-model at a daily scale, outperforming the M_{RC} sediment

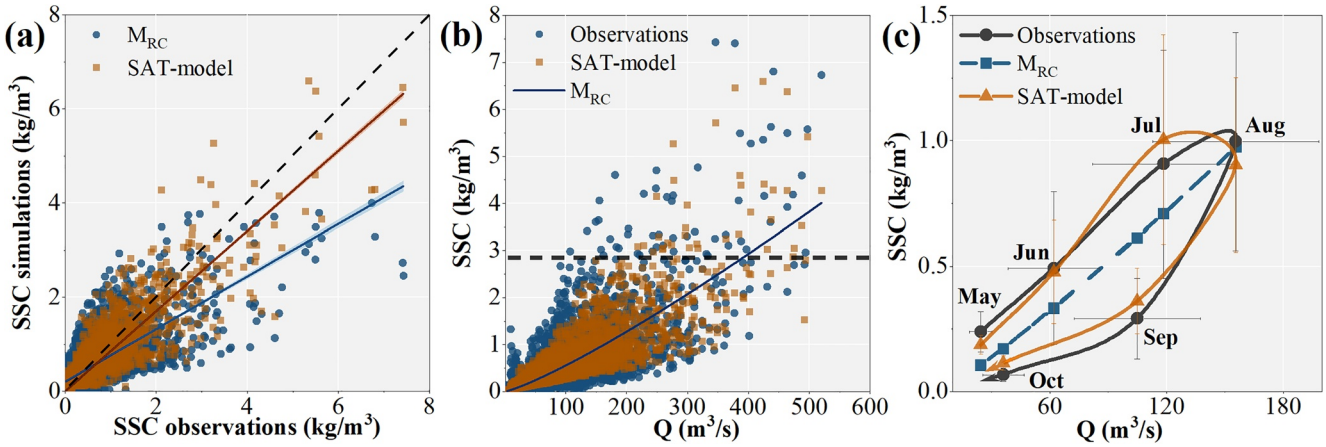

Figure 6. Comparison of model performance between the SAT-model (M_{SAT}) and the sediment rating curve (M_{RC}). (a) Relationship between simulated and observed SSC for the M_{SAT} and M_{RC}. The red line represents the linear regression between estimated and observed SSC for M_{SAT}, with a slope of 0.85 ± 0.006 (R^2 = 0.77). The blue line is the linear regression between estimated and observed SSC for M_{RC}, with a slope of 0.55 ± 0.008 (R^2 = 0.54). (b) Scatter plot between SSC and discharge (Q). Values above the red dash line corresponds to the top 1 percentile of SSC (2.9 kg/m³). (c) Hysteresis between monthly SSC and Q.

rating curve (0.74; Figure 6a). The SAT-model can also reproduce the scatters in SSC-Q relationships by accounting for the changing sediment availability (Figures 6b and 7a–7c). Additionally, SSC peaks (defined as local SSC maxima) and extreme values (e.g., SSC over 2.9 kg/m³) are better represented by the SAT-model, which are clearly underestimated by the sediment rating curve with most of the estimations below the 1:1 line (Figure S6 in Supporting Information S1). Although significant improvements are also found in models only integrating the impact of temperature or runoff surge (M_T and M_F), the SAT-model still outperforms these by considering the coupled impact of temperatures, runoff surge, and sediment storage (Table 2).

Moreover, the SAT-model captures the seasonality in sediment transport and reproduces the hysteretic pattern in the monthly SSC-Q relationship, with similar monthly standard deviations between the estimated and observed SSC (Figure 6c). In addition to the factors of temperature and runoff surge, the inclusion of the geomorphic exhaustion index renders the SAT-model to reproduce the sediment seasonality (a clockwise hysteresis and lower sediment availability in autumn; Figure 4a). For example, at seasonal scale, the M_{TF} without the geomorphic exhaustion index significantly overestimates the SSC in autumn (by 56%) and underestimates the SSC in spring (by 30%; Figure S7 and Table S3 in Supporting Information S1). By contrast, the SAT-model effectively reduces the overestimation in SSC in autumn and the underestimation in SSC in spring and summer that is simulated by the M_{RC} sediment rating curve (Table 3 and Figure 7). In particular, the SAT-model shows the largest improvement in autumn and explains 78% of its variance (Table 3). The relative error (RE) in the autumn SSC is controlled within 32% by the SAT-model, which is overestimated by 119% when using the M_{RC} rating curve (Figures 7c and 7f). Additionally, the SAT-model shows a significant improvement in the R^2 in summer (from 0.49 to 0.71; Table 3). The SSC peaks in summer are also effectively captured by the SAT-model, with no significant overestimation or underestimation (RE ~ 0%; Figures 7b and 7e). The underestimation of spring SSC in the rating curve is also significantly reduced by the SAT-model, from 40% to 10% (Table 3, Figures 7a and 7d).

Table 3
Comparison of Seasonal Performance Between Rating Curve and Sediment-Availability-Transport (SAT)-Model

Season	Model	NSE	RE (%)	R^2
Spring	M_{RC}	0.42	−40	0.57
	M_{SAT}	0.67	−10	0.69
Summer	M_{RC}	0.47	−12	0.49
	M_{SAT}	0.72	0	0.71
Autumn	M_{RC}	−0.51	119	0.71
	M_{SAT}	0.73	32	0.78

Note. NSE, Nash-Sutcliffe efficiency; RE, relative error.

5. Validation of the SAT-Model Performance

5.1. The Robustness and Cross-Validation of the SAT-Model

The improvement of the SAT-model compared with the M_{RC} sediment rating curve is proved to be significant and robust as evidenced by the 10 times of cross-validation (Table 4), with a net improvement of the R^2 of 0.2 for the SAT-model compared with the M_{RC} rating curve. We also test

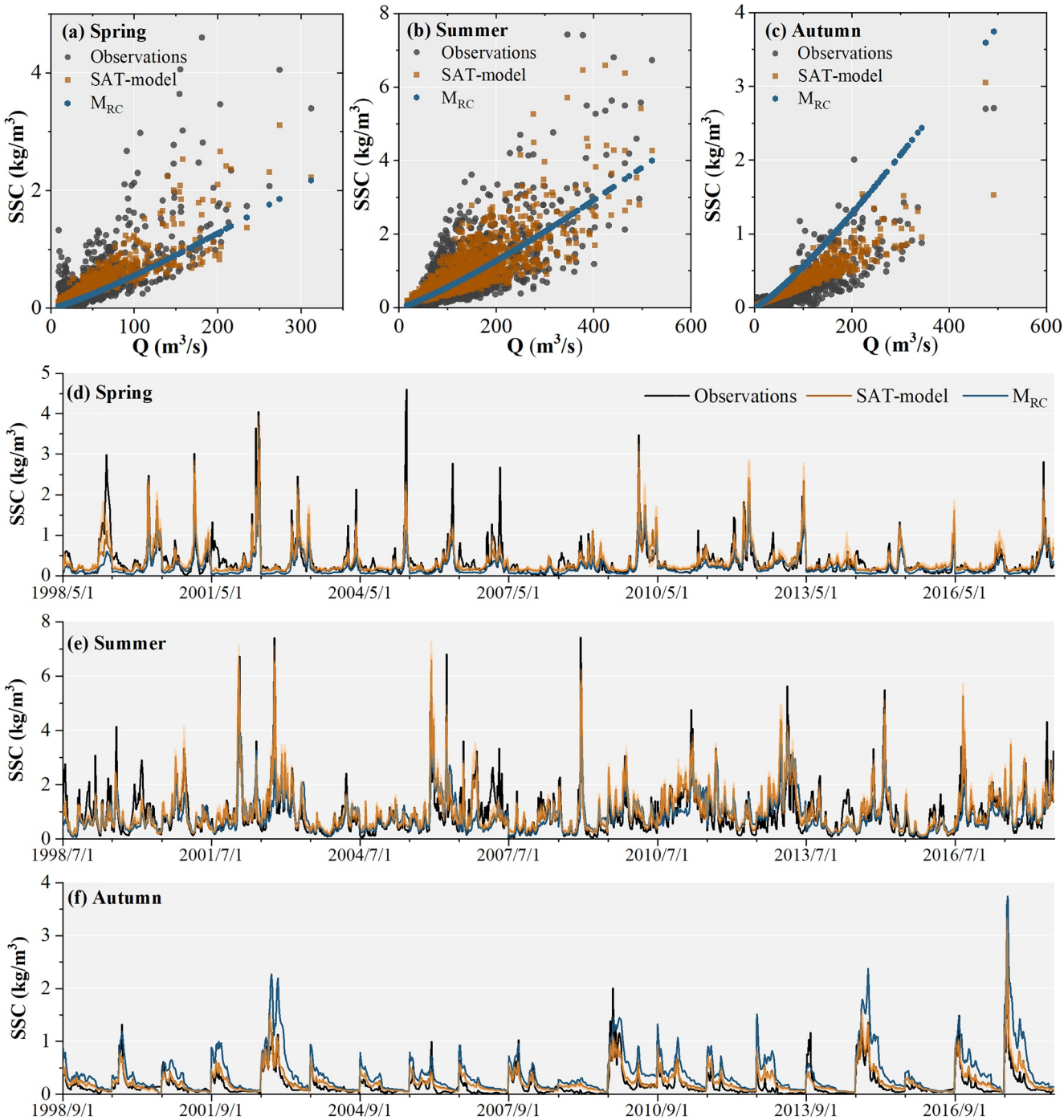

Figure 7. Daily observed and simulated suspended sediment concentration by M_{SAT} and M_{RC} in (a), (d) Spring, (b), (e) Summer and (c), (f) Autumn during 1998–2017. The light orange shaded area in Figures 7d–7f are the standard error (SE) in simulations from M_{SAT}. See Table 3 for the Nash-Sutcliffe efficiency, relative error, and R^2.

the model performance under abrupt change of the hydroclimate; this can be done because the SAT-model and the M_{RC} sediment rating curve were calibrated by data before the abrupt-change year (1997) and validated by data after the abrupt-change year. Overall, the SAT-model demonstrates robust long-term projection capacity (Table 5). The calibrated SAT-model can capture the SSC variability and simulate the long-term SSC evolution under climate change, with NSEs over 0.7 before and after hydroclimate abrupt change.

Table 4
Comparison of Model Performance by 10-Time Cross-Validation

	SAT-model		Sediment rating curve	
Metrics	Calibration	Validation	Calibration	Validation
NSE	0.76 ± 0.010	0.72 ± 0.012	0.56 ± 0.010	0.53 ± 0.006
RE (%)	1.43 ± 0.266	3.84 ± 2.292	−3.34 ± 0.784	−2.18 ± 3.050
R^2	0.76 ± 0.010	0.74 ± 0.006	0.56 ± 0.010	0.54 ± 0.004

Note. The calibration period is the randomly selected 10 years during 1985–2017 (detailed selections are shown in Table S4 in Supporting Information S1). The validation period is the remaining 23 years from 1985 to 2017. For each model, such cross-validation is repeated 10 times. The indices here are recorded as the mean value ± standard error of the 10 tests. For the indices of each test for the SAT-model and the M_{RC} sediment rating curve, see Tables S5 and S6 in Supporting Information S1, respectively.

However, the performance of M_{RC} sediment rating curve is unstable and considerably impacted by climate change, resulting in a significantly reduced model performance after the abrupt-change year (NSE reduces from 0.61 to 0.29).

5.2. Reproduction of Event Scale SSC-*Q* Hysteretic Patterns

The SAT-model can reproduce various event-scale SSC-*Q* hysteretic patterns, including clockwise (C), counter-clockwise (C-C), figure-eight (E), counter-figure-eight (C-E) and more complex hysteresis loops (Figure 8 and Figure S8 in Supporting Information S1). In cold environments, peak SSC events can be caused by different processes induced by glacier-snow melt, permafrost thawing and rainfall (Costa et al., 2018; Li et al., 2021a). The various drivers and antecedent situations (e.g., several consecutive events) can lead to complex event-scale SSC-*Q* hysteresis. The SAT-model can effectively simulate such hysteresis by integrating the coupled impacts of the basin temperature and runoff surge (Figure 8c and Figure S8c in Supporting Information S1).

Taking the year of 2002 (the highest mean annual SSC; Figure 1e) as an example, 12 distinct peak SSC events are reproduced by the SAT-model (Figure 8c). The simulated hysteresis loops have identical patterns and similar SSC magnitudes compared to the observations. Specifically, the dominant control on spring SSC peaks is the melting of the snowpack (Figure 8a). Through capturing the increases of temperature and discharge associated with snowmelt in the rising limb, the SAT-model simulated the spring clockwise (C) loops (events 1–2). In summer, SSC pulses can be caused by multiple drivers and are characterized by successive peaks (events 3–10). For event 4, the figure-eight (E) loop is mainly caused by several intermittent rainfall events. For instance, the first rainfall event in the beginning led to surges of discharge and SSC. The strong and transient rainstorm events (over 15 mm/day) associated with peak discharges maintained the sediment supply for a short time in the falling limb. Through capturing the "rising-cease-rising" trend of discharge, this figure-eight loop was reproduced by the SAT-model. Besides, the counter-clockwise loop (C-C) was also found in summer (event 8). This is most likely caused by the insufficient sediment at the beginning due to sediment exhaustion after consecutive peaks, and a delayed sediment supply from the thawing permafrost and melting glaciers in the more upper reaches of the catchment (Figure 8a). The SAT-model reproduced this event by integrating the antecedent temperature conditions and the slow discharge increase at the start of the event. Autumn SSC peaks are mainly the result of rainfall, associated with snowmelt (events 11–12). Especially, the first small peak in event 11 caused by the melting snow was effectively captured by the temperature-term in the SAT-model. These event-scale SSC-*Q* hysteresis are entirely missed by the M_{RC} sediment rating curve, resulting in obvious deviations in sediment estimations (Figure 8c). Despite the overall outperformance of the SAT-model, the overestimation of sediment availability can be found in consecutive peaks following an earlier higher peak (e.g., events 3 and 7). The higher discharge in previous peaks and the short low-flow period between events can lead to excessive sediment depletion and delayed sediment recovery, and thus cause insufficient sediment availability in the following events.

Table 5
Overall Model Performance Before and After the Hydroclimate Abrupt Change

	SAT-model		Sediment rating curve	
Metrics	Calibration	Validation	Calibration	Validation
NSE	0.74	0.71	0.61	0.29
RE	−5%	21%	−4%	42%
R^2	0.74	0.77	0.61	0.54

Note. The calibration period is 1985–1997 (before the abrupt hydroclimate). The validation period is 1998–2017 (after the abrupt hydroclimate change).

Moreover, The SAT-model successfully reproduced the magnitude and hysteresis of extreme sediment events (Figure 9). Those short lasting extreme events containing high sediment loads are important in shaping channel forms (Li et al., 2019). However, they are often largely underestimated by using the M_{RC} sediment rating curve. In Tuotuohe, the top-10 SSC events represent only 3% of the total days but contribute 21% of the total suspended sediment load from 1998 to 2017 (Table S7 in Supporting Information S1). Clockwise hysteresis is observed during those events. The higher SSC in the rising limb is captured by the SAT-model, even in the events with multiple peaks and a more complex hysteresis pattern (e.g., events 6,7,10 in Figure 9). The magnitude of peak SSC is

10.1029/2021WR030690

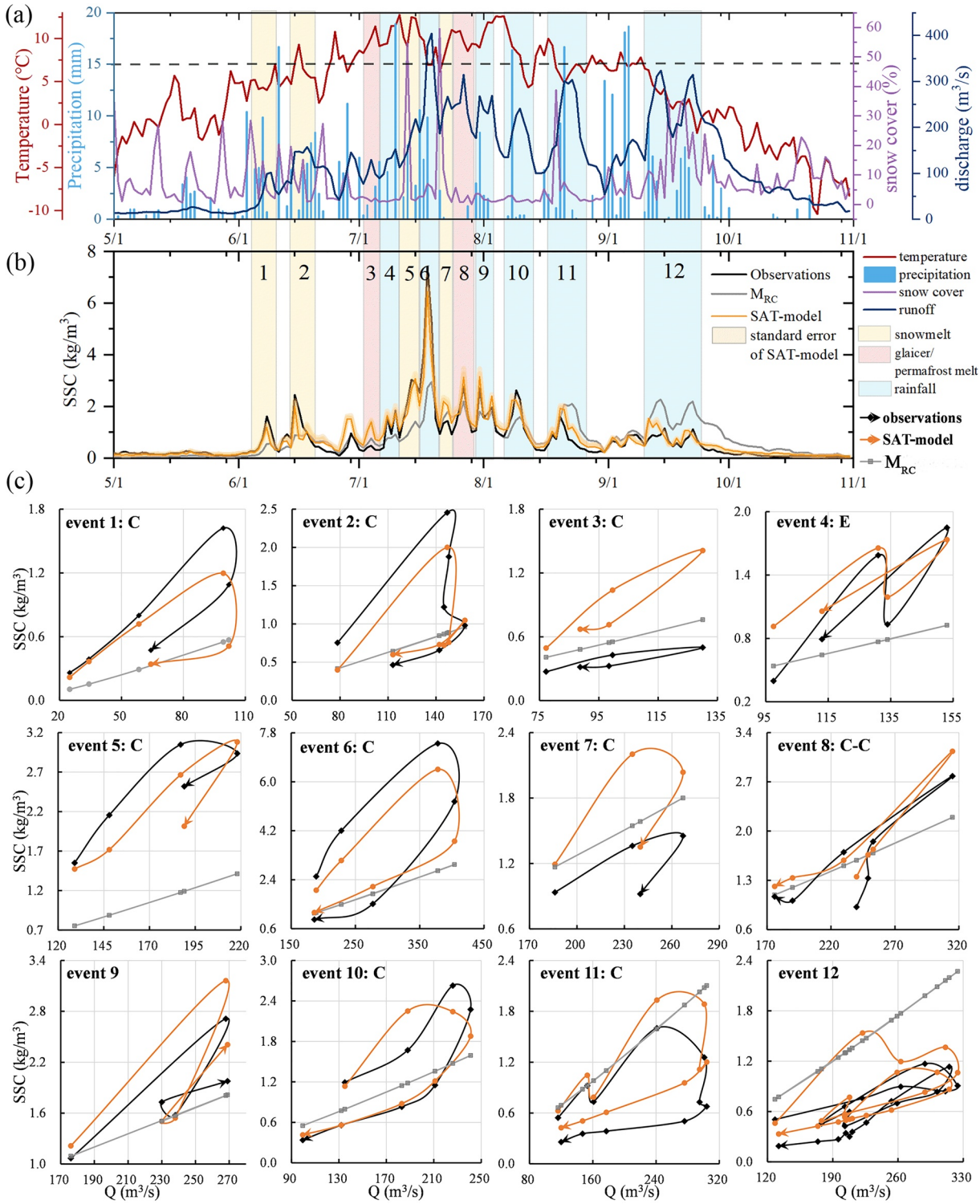

Figure 8. Hysteresis of peak suspended sediment concentration (SSC) events for the hydrological year of 2002. (a) Control parameters (air temperature, precipitation, snow cover, and discharge) of daily SSC. Values above the gray dash line represents the top 1 percentile of precipitation (15 mm/day). 1–12 represent 12 peak SSC events caused by different controls, namely, snowmelt, glacier/permafrost melt, and rainfall. (b) Observed and simulated SSC for 2002. The shaded area represents the standard error (SE) of the simulated SSC by the SAT-model. (c) Simulated and observed hysteresis loops of 12 peak SSC events in 2002. *Q* is discharge (m^3/s). Events are categorized by the dominant drivers. Specifically, the events with a sudden decline in snow coverage and no extreme rainfall events (over 15 mm/day) are identified as snowmelt events. Events with extreme or relatively high rainfall are identified as rainfall events. Events with relatively high temperature but low precipitation and little snow coverage reduction are identified as glacier/permafrost melt events.

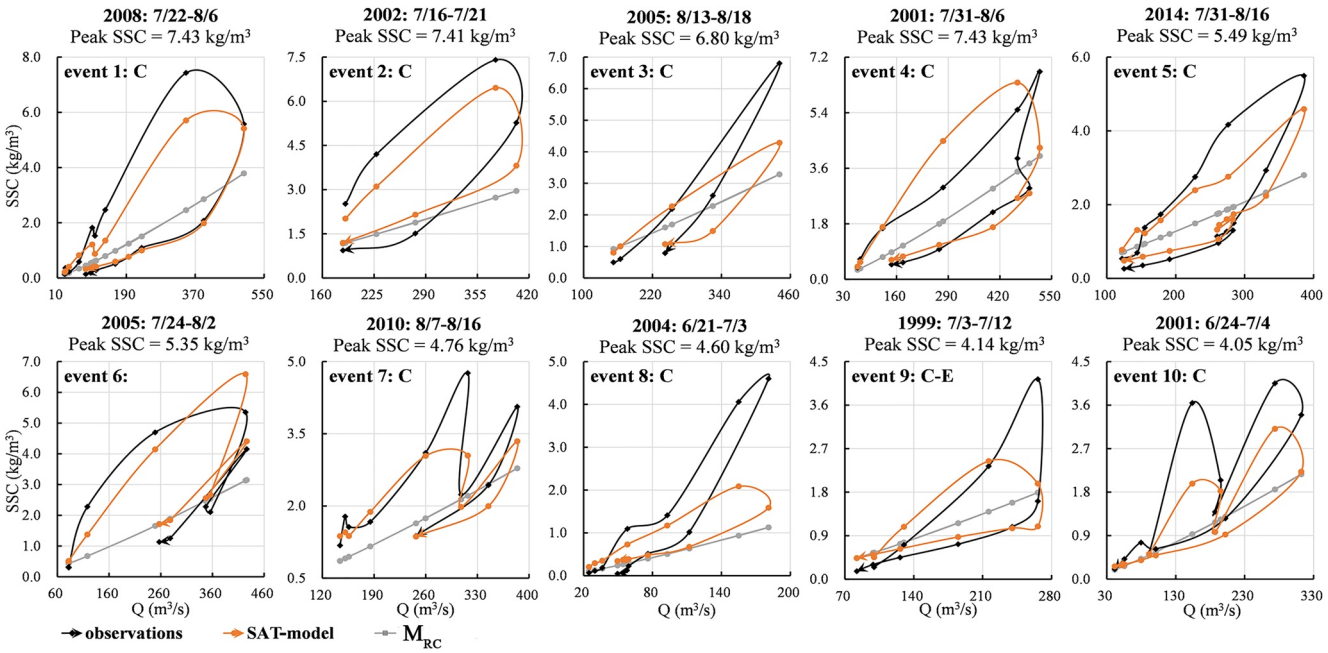

Figure 9. Simulated and observed hysteresis loops of the top-10 extreme suspended sediment concentration events over the period of 1998–2017.

reasonably estimated by the SAT-model, ranging from 2.09 to 6.59 (Table S7 in Supporting Information S1). Despite the underestimation of overall sediment load for the extreme events (~17%), the SAT-model still significantly outperforms the M_{RC} rating curve (~32%; Table S7 in Supporting Information S1). The underestimation is caused by the underestimated sediment availability during the extreme events. These extreme

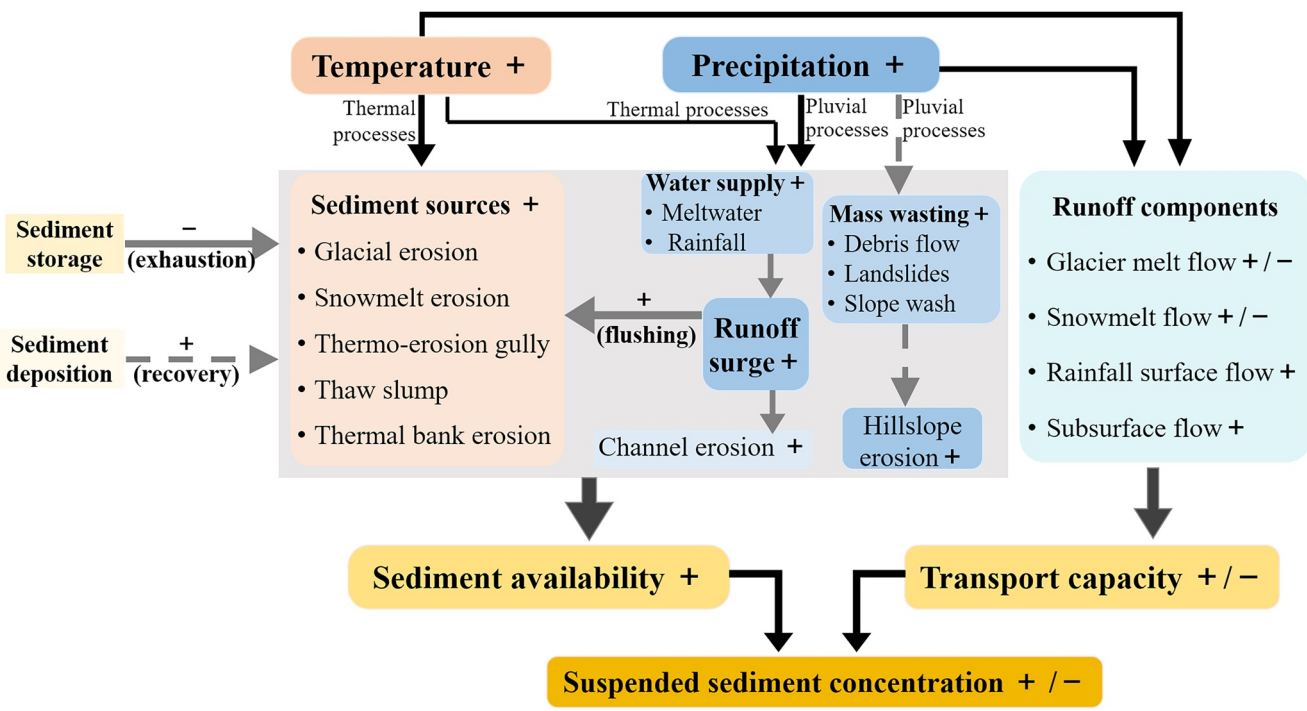

Figure 10. Conceptual framework of the response of suspended sediment concentration to climate change in the sediment-availability-transport (SAT)-model. The gray-dash arrow represents the process that are not explicitly considered in the presented SAT-model.

events are characterized by large runoff surge and relatively high temperature (Figure 5), which may trigger exceptional erosional processes after certain thresholds are exceeded (Figure 5c).

6. Response of Fluvial Sediment to Climate Change Simulated by the SAT-Model

We introduce a conceptual framework to understand how fluvial sediment responds to climate change in cold environments (Figure 10). The rising SSC is caused by the elevated sediment availability and increased transport capacity in a warmer and wetter climate. The changes in sediment availability in cold basins are controlled not only by thermally activated sediment sources from slopes and riverbanks, but also by enhanced fluvial erosion (Li et al., 2021a; Syvitski, 2002). In the SAT-model, such thermally erosional processes are captured by basin temperature and the enhanced fluvial erosion is captured by runoff surge. In cold basins, runoff surge can be induced by both glacier-snow meltwater (Khanal et al., 2021) and effective rainfall flow (Figure 10); this leads to a relatively independent relationship between runoff surge and temperature especially for extreme sediment events (Figures 5a and 5c). Therefore, runoff surge provides a better representation of fluvial processes when compared to precipitation (Figure S5 in Supporting Information S1). Furthermore, the effects of runoff surge-related fluvial erosion and the temperature-related thermal erosion can interact and amplify each other (Godin et al., 2019; Kokelj et al., 2015).

The ever-evolving sediment availability in cold environments is driven by various temperature-sensitive erosion processes such as glacial erosion, snowmelt erosion, permafrost erosion, and thermal bank erosion. With rising temperatures, the increasing glacier meltwater not only transports glacial sediment downstream, but also strengthens the hydro-connectivity in the pro-glacial area (Lane et al., 2017). Snowpack melting and permafrost thawing expand the snow-free and erodible landscapes, which further increases the erosivity of rainfall and meltwater (Costa et al., 2018; Li et al., 2021a). The expanded erodible areas in the warm season can be found in Tuotuohe through comparing Google earth images in winter and summer (Figure 11 and Figure S10 in Supporting Information S1). The formation of thermo-erosion gully enhances the sediment connectivity between river channels and relatively distant slope sediment sources (Figure 11; Taylor et al., 2018; Wohl et al., 2019). Gullies rely on the water supply to activate the erosion processes and evolve into contributing tributaries (Godin et al., 2014; Rodzik et al., 2009). For instance, the increased gully runoff transports the sediment generated on the slopes and gullies downstream during the melting or rainy season (the blue symbols in Figure 11a). Additionally, thaw slumps can be initiated by thawing of exposed ground ice when temperature increases (Kokelj et al., 2013). Initiation and activation of thaw slumps are highly sensitive to temperature; they can be stabilized when temperature is below 0°C and reactivated by above freezing temperatures and the melting ground ice acts as water source (Lewkowicz & Way, 2019). They are usually near the thermo-erosion gullies and river channels, providing a bulk of sediments to rivers by large-extent and long-lasting mass movements (Lafrenière & Lamoureux, 2019). Several large-scale channel-connected thaw slumps (extending over 1 km) have been found in Tuotuohe (Figures 11b–11d). Furthermore, the rapid increase of discharge can accelerate the degradation of permafrost along the river, and trigger thermal bank erosion (Zheng et al., 2019). In Tuotuohe, thermal bank erosion can be found during the summer (Figure 11e), often associated with thaw slumps (Figure 11c). Although the hillslope erosion trigger by intense rainfall has not been simulated explicitly in the current SAT-model (Figure 10), sediments from mass wasting (e.g., landslides and debris flows) may be important sediment sources in cold environments (Hirschberg et al., 2021; Simoni et al., 2020), and may need to be considered separately in future.

In the SAT-model, transport capacity is represented by the total runoff and the glacier-snow-permafrost erosion is captured by more generic variables (e.g., basin temperature and runoff surge; Figure 10). Although these proxies may obscure the individual contribution of glacier, snow, or permafrost erosion, it enables the SAT-model to reproduce the SSC peaks caused by various factors (Figure 8 and Figure S8 in Supporting Information S1) and to be applied in other cold basins of the Tibetan Plateau and (sub)Arctic regions. In (sub) Arctic basins, their fluvial sediment fluxes are also sensitive to global warming and increased runoff from elevated meltwater and rainfall flow, despite the relatively low sediment yield limited by hard lithology, cold climate and thick tundra (Li et al., 2021b). The increased thermally activated sediment sources and sediment connectivity boosted by fluvial events have been widely observed in the Arctic (Beel et al., 2020, 2021; Lewkowicz & Way, 2019; Syvitski, 2002).

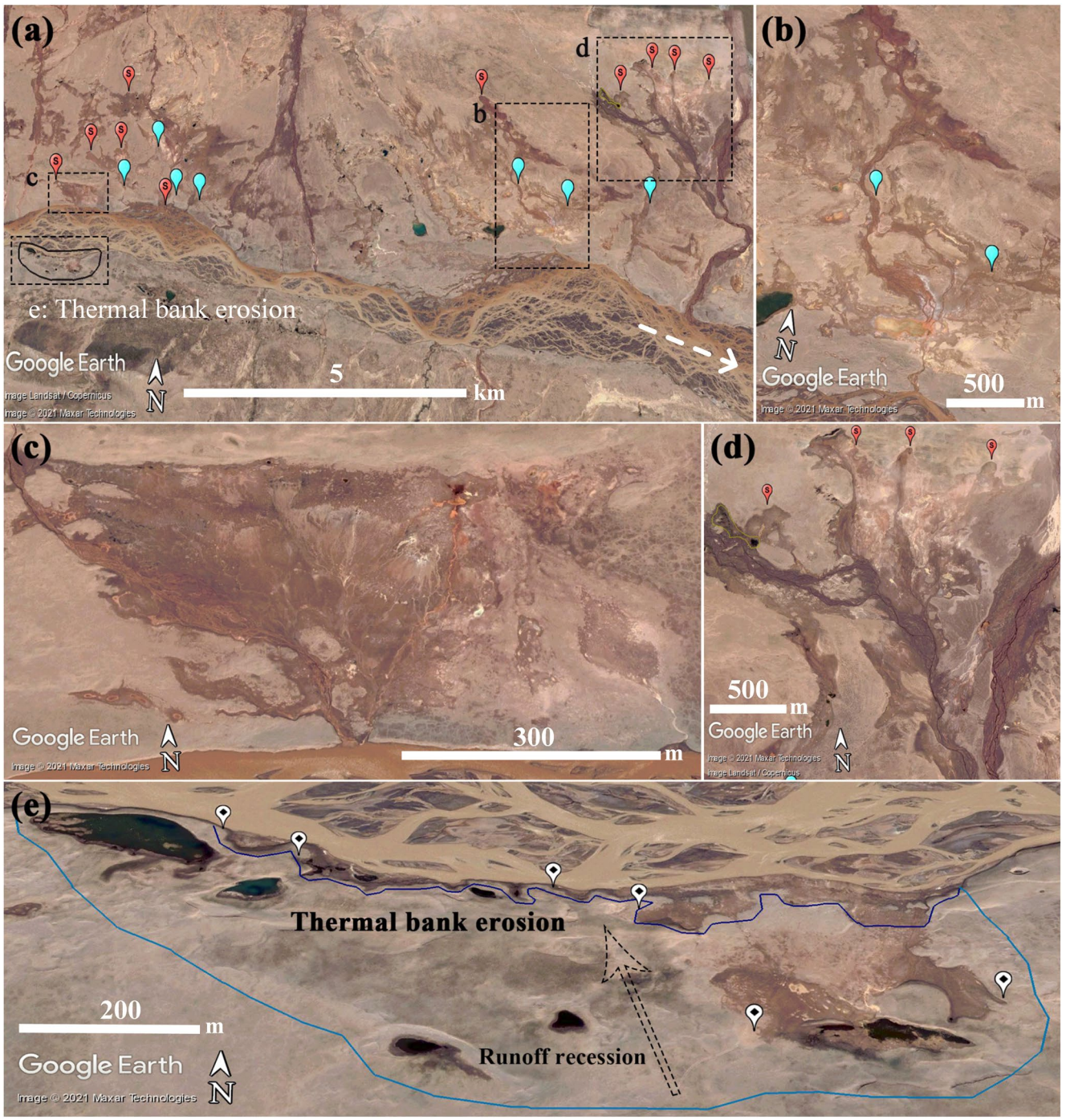

Figure 11. Main sediment sources and the erodible landscapes of Tuotuohe basin in summer based on Google earth images. This figure is a small area in Tuotuohe covered by high quality images and the location relative to the entire Tuotuohe basin is shown in Figure S9 in Supporting Information S1. The corresponding landscapes in winter is shown in Figure S10 in Supporting Information S1. Reference data from Google Earth: Google Earth Imagery 2006 (© 2021 Maxar Technologies), and dated 2006/8/21. Light blue marks represent gullies. Red marks represent thaw slumps. In Figure 11e, the white marks represent several apparent small thermal bank erosions. The light blue line delineates the extent of floodplain erosion and the dark blue line delineates the extent of bank erosion.

In the next step, transport capacity of runoff components can be separated in the SAT-model to further disentangle the snowmelt erosion and glacier melt erosion (Figure 10). This may help to differentiate the individual contribution of various erosion processes and the different responses of runoff components to climate change, like the decreased snowmelt flow and increased rainfall flow in a warming climate (Khanal et al., 2021; Wang et al., 2021). Additionally, in the SAT-model, the impact of sediment storage of previous years on sediment availability is considered by a geomorphic exhaustion index within a hydrological year (Figure 10). Nevertheless, event-scale sediment storage changes (e.g., exhaustion and recovery between peak SSC events) are not simulated in the current version of the SAT-model, something that needs to be further analyzed and considered.

Based on the response framework of SSC to climate change (Figure 10), the SAT-model can be generalized as a conceptual model, that is, Equation 4. This conceptual model encompasses multiple proxies: changes in new available sediment sources due to cryosphere degradation (g), erosivity enhanced by runoff surge (f), and sediment storage regulated by storage exhaustion and recovery (h). Moreover, different proxies can be freely selected/adjusted for a certain basin to incorporate the catchment-specific drivers explicitly, depending on specific landscape characteristics and sediment transport mechanisms. For instance, rainfall-related variables can be incorporated into the function of g to explicitly account for the hillslope erosion triggered by rainstorms in basins commonly associate with mass wasting events. Thus, this conceptual model can be applied in other cold basins where there are different erosion mechanisms.

$$\mathrm{SSC} = h\left(\mathrm{storage}\right) \times a_1 \times Q^{g\left(\mathrm{newavailablesources}\right)} + h\left(\mathrm{storage}\right) \times f\left(\mathrm{erosivity}\right) \times Q^{b} + a_2 \times Q \tag{4}$$

where, SSC and Q are suspended sediment concentration (kg/m^3) and discharge (m^3/s), respectively. a_n and b are the fitting parameters, which need to be adjusted for specific basins.

In this model framework, we mainly focus on the direct impact of climate change. However, the changing climate can also indirectly impact erosion and sediment transport through altering the landcover and the vegetation (Lian et al., 2020; Wu et al., 2020). These and other indirect impacts should be investigated in future to better understand long term sediment impacts of climate change.

7. Conclusions

The SAT model presented in this study can robustly reproduce the long-term evolution, seasonality and various event-scale hysteresis of SSC in a representative cold basin (Tuotuohe basin on the Tibetan Plateau) by simulating the dynamic sediment availability regulated by coupled thermal and fluvial processes.

In the SAT-model, fluvial transport capacity is represented by total runoff (Q). The dynamic sediment availability is represented by the basin temperature and runoff surge. With climate warming, glacier-snow-permafrost melting enlarges the unstable and erodible landscapes (e.g., thaw slumps and thermal bank erosion) and enhances the sediment connectivity between channels and slopes (e.g., formation of snowmelt gullies and thermo-erosion gullies), providing elevated sediment sources. These thermal processes are found to be best captured by the 8-day average temperature (with 1-week antecedent conditions), associated with an exponential amplification of SSC. Additionally, erosion processes can be initiated and enhanced by the increase in runoff from elevated rainfall and meltwater, associated with strengthened flushing and channel scouring. Such fluvial processes are found to be best captured by the 2-day discharge increase and show a linear amplification of SSC. Furthermore, the exhaustion of sediment storage within a hydrological year is integrated into the SAT-model to modify the sediment availability. Moreover, the SSC-Q hysteresis in Tuotuohe displays various patterns with clockwise, counter-clockwise, figure-eight, counter-figure-eight and more complex loops. All these patterns can be reproduced by the SAT-model. The SAT-model can explain over 75% of long-term SSC variance, outperforming the M_{RC} sediment rating curve by 20%. The performance of the SAT-model is robust, even under an abrupt hydroclimate change, with a Nash-Sutcliffe efficiency coefficient ranging from 0.76 to 0.71 during the calibration and validation periods, respectively.

Overall, the SAT-model shows merits over the M_{RC} sediment rating curve or other event-scale hysteresis models in the following aspects: (a) having strong capability to robustly simulate long-term SSC evolution and short-term SSC-Q dynamics under a changing climate; (b) possessing a straightforward and user-friendly model function with clear physical meanings; and (c) providing a framework that can be applied to other

cold basins and continuously developed to incorporate more processes explicitly. The accelerating melting of the cryosphere due to global warming highlights the increasing need to consider thermally controlled sediment sources in sediment transport models. The SAT-model not only advances our understanding of sediment transport mechanisms coupled by thermal and fluvial processes, but also provides a model framework to simulate and project sediment load changes in other cold basins. The erosion proxies in the model framework can be added, removed or reconstructed to account for the catchment-specific sediment drivers.

Data Availability Statement

Precipitation and air temperature data were retrieved from the National Meteorological Information Center (http://data.cma.cn/en). Discharge and sediment data were sourced and available from the Qinghai Hydrology Bureau and the Changjiang Water Resources Commission (http://www.cjh.com.cn/en/). The snow cover data were derived from the MODIS Terra/Aqua Snow Cover Daily L3 Global 500-m Grid (MO/YD10A1) data set (https://nsidc.org/data/MOD10A1). Other data such as land cover, river networks, glaciers, and permafrost are available at the National Tibetan Plateau Data Center (http://www.tpdc.ac.cn/en/).

Acknowledgments
This study was supported by the MOE grants and the National University of Singapore (R-109-000-273-112, R-109-000-227-115, and NUS President's Graduate Fellowship). D. Li acknowledges IPCC Scholarship Award (jointly founded by the IPCC and Cuomo Foundation). Y. Zhou acknowledges Central Public-interest Scientific Institution Basal Research Fund (CKSF2021485; CKSF2021743).

References

Ahn, K.-H., & Steinschneider, S. (2018). Time-varying suspended sediment-discharge rating curves to estimate climate impacts on fluvial sediment transport. *Hydrological Processes*, *32*(1), 102–117. https://doi.org/10.1002/hyp.11402

Ahn, K. H., Yellen, B., & Steinschneider, S. (2017). Dynamic linear models to explore time-varying suspended sediment-discharge rating curves. *Water Resources Research*, *53*(6), 4802–4820. https://doi.org/10.1002/2017wr020381

Ara Rahman, S., & Chakrabarty, D. (2020). Sediment transport modelling in an alluvial river with artificial neural network. *Journal of Hydrology*, *588*, 125056. https://doi.org/10.1016/j.jhydrol.2020.125056

Asselman, N. E. M. (2000). Fitting and interpretation of sediment rating curves. *Journal of Hydrology*, *234*(3), 228–248. https://doi.org/10.1016/S0022-1694(00)00253-5

Beel, C. R., Heslop, J. K., Orwin, J. F., Pope, M. A., Schevers, A. J., Hung, J. K. Y., et al. (2021). Emerging dominance of summer rainfall driving High Arctic terrestrial-aquatic connectivity. *Nature Communications*, *12*(1), 1448. https://doi.org/10.1038/s41467-021-21759-3

Beel, C. R., Lamoureux, S. F., Orwin, J. F., Pope, M. A., Lafrenière, M. J., & Scott, N. A. (2020). Differential impact of thermal and physical permafrost disturbances on High Arctic dissolved and particulate fluvial fluxes. *Scientific Reports*, *10*(1), 11836. https://doi.org/10.1038/s41598-020-68824-3

Bendixen, M., Lønsmann Iversen, L., Anker Bjørk, A., Elberling, B., Westergaard-Nielsen, A., Overeem, I., et al. (2017). Delta progradation in Greenland driven by increasing glacial mass loss. *Nature*, *550*(7674), 101–104. https://doi.org/10.1038/nature23873

Best, J. (2019). Anthropogenic stresses on the world's big rivers. *Nature Geoscience*, *12*(1), 7–21. https://doi.org/10.1038/s41561-018-0262-x

Bolch, T., Shea, J. M., Liu, S., Azam, F. M., Gao, Y., Gruber, S., et al. (2019). Status and change of the cryosphere in the extended Hindu Kush Himalaya Region. In P. Wester, A. Mishra, A. Mukherji, & A. B. Shrestha (Eds.), *The Hindu Kush Himalaya assessment: Mountains, climate change, sustainability and people* (pp. 209–255). Springer International Publishing. https://doi.org/10.1007/978-3-319-92288-1_7

Costa, A., Molnar, P., Stutenbecker, L., Bakker, M., Silva, T. A., Schlunegger, F., et al. (2018). Temperature signal in suspended sediment export from an Alpine catchment. *Hydrology and Earth System Sciences*, *22*(1), 509–528. https://doi.org/10.5194/hess-22-509-2018

Darby, S. E., Hackney, C. R., Leyland, J., Kummu, M., Lauri, H., Parsons, D. R., et al. (2016). Fluvial sediment supply to a mega-delta reduced by shifting tropical-cyclone activity. *Nature*, *539*(7628), 276–279. https://doi.org/10.1038/nature19809

Delaney, I., & Adhikari, S. (2020). Increased subglacial sediment discharge in a warming climate: Consideration of ice dynamics, glacial erosion, and fluvial sediment transport. *Geophysical Research Letters*, *47*(7). https://doi.org/10.1029/2019gl085672

Du, Y., Berndtsson, R., An, D., Zhang, L., Yuan, F., & Hao, Z. (2019). Integrated large-scale circulation impact on rainy season precipitation in the source region of the Yangtze River. *International Journal of Climatology*, *40*(4), 2285–2295. https://doi.org/10.1002/joc.6332

Duvert, C., Gratiot, N., Evrard, O., Navratil, O., Némery, J., Prat, C., & Esteves, M. (2010). Drivers of erosion and suspended sediment transport in three headwater catchments of the Mexican Central Highlands. *Geomo*, *123*(3–4), 243–256. https://doi.org/10.1016/j.geomorph.2010.07.016

Eder, A., Strauss, P., Krueger, T., & Quinton, J. N. (2010). Comparative calculation of suspended sediment loads with respect to hysteresis effects (in the Petzenkirchen catchment, Austria). *Journal of Hydrology*, *389*(1–2), 168–176. https://doi.org/10.1016/j.jhydrol.2010.05.043

Gan, M., Chen, C. L. P., Chen, G., & Chen, L. (2018). On some separated algorithms for separable nonlinear least squares problems. *IEEE Transactions on Cybernetics*, *48*(10), 2866–2874. https://doi.org/10.1109/TCYB.2017.2751558

Godin, E., Fortier, D., & Coulombe, S. (2014). Effects of thermo-erosion gullying on hydrologic flow networks, discharge and soil loss. *Environmental Research Letters*, *9*(10), 105010. https://doi.org/10.1088/1748-9326/9/10/105010

Godin, E., Osinski, G. R., Harrison, T. N., Pontefract, A., & Zanetti, M. (2019). Geomorphology of Gullies at Thomas Lee Inlet, Devon Island, Canadian High Arctic. *Permafrost and Periglacial Processes*, *30*(1), 19–34. https://doi.org/10.1002/ppp.1992

Hilton, R. G., Galy, A., Hovius, N., Chen, M.-C., Horng, M.-J., & Chen, H. (2008). Tropical-cyclone-driven erosion of the terrestrial biosphere from mountains. *Nature Geoscience*, *1*(11), 759–762. https://doi.org/10.1038/ngeo333

Hirschberg, J., Fatichi, S., Bennett, G. L., McArdell, B. W., Peleg, N., Lane, S. N., et al. (2021). Climate change impacts on sediment yield and debris-flow activity in an alpine catchment. *Journal of Geophysical Research: Earth Surface*, *126*(1). https://doi.org/10.1029/2020jf005739

Jaeger, J. M., & Koppes, M. N. (2016). The role of the cryosphere in source-to-sink systems. *Earth-Science Reviews*, *153*, 43–76. https://doi.org/10.1016/j.earscirev.2015.09.011

Juez, C., Hassan, M. A., & Franca, M. J. (2018). The origin of fine sediment determines the observations of suspended sediment fluxes under unsteady flow conditions. *Water Resources Research*, *54*(8), 5654–5669. https://doi.org/10.1029/2018wr022982

Kettner, A. J., & Syvitski, J. P. M. (2008). HydroTrend v.3.0: A climate-driven hydrological transport model that simulates discharge and sediment load leaving a river system. *Computers & Geosciences*, *34*(10), 1170–1183. https://doi.org/10.1016/j.cageo.2008.02.008

Khanal, S., Lutz, A. F., Kraaijenbrink, P. D. A., van den Hurk, B., Yao, T., & Immerzeel, W. W. (2021). Variable 21st century climate change response for rivers in High Mountain Asia at seasonal to decadal time scales. *Water Resources Research*, *57*(5). https://doi.org/10.1029/2020wr029266

Knight, J., & Harrison, S. (2012). The impacts of climate change on terrestrial Earth surface systems. *Nature Climate Change*, *3*(1), 24–29. https://doi.org/10.1038/nclimate1660

Kokelj, S. V., Lacelle, D., Lantz, T. C., Tunnicliffe, J., Malone, L., Clark, I. D., & Chin, K. S. (2013). Thawing of massive ground ice in mega slumps drives increases in stream sediment and solute flux across a range of watershed scales. *Journal of Geophysical Research: Earth Surface*, *118*(2), 681–692. https://doi.org/10.1002/jgrf.20063

Kokelj, S. V., Tunnicliffe, J., Lacelle, D., Lantz, T. C., Chin, K. S., & Fraser, R. (2015). Increased precipitation drives mega slump development and destabilization of ice-rich permafrost terrain, northwestern Canada. *Global and Planetary Change*, *129*, 56–68. https://doi.org/10.1016/j.gloplacha.2015.02.008

Lafrenière, M. J., & Lamoureux, S. F. (2019). Effects of changing permafrost conditions on hydrological processes and fluvial fluxes. *Earth-Science Reviews*, *191*, 212–223. https://doi.org/10.1016/j.earscirev.2019.02.018

Lane, S. N., Bakker, M., Gabbud, C., Micheletti, N., & Saugy, J.-N. (2017). Sediment export, transient landscape response and catchment-scale connectivity following rapid climate warming and Alpine glacier recession. *Geomo*, *277*, 210–227. https://doi.org/10.1016/j.geomorph.2016.02.015

Langlois, J. L., Johnson, D. W., & Mehuys, G. R. (2005). Suspended sediment dynamics associated with snowmelt runoff in a small mountain stream of Lake Tahoe (Nevada). *Hydrological Processes*, *19*(18), 3569–3580. https://doi.org/10.1002/hyp.5844

Lefrançois, J., Grimaldi, C., Gascuel-Odoux, C., & Gilliet, N. (2007). Suspended sediment and discharge relationships to identify bank degradation as a main sediment source on small agricultural catchments. *Hydrological Processes*, *21*(21), 2923–2933. https://doi.org/10.1002/hyp.6509

Lewkowicz, A. G., & Way, R. G. (2019). Extremes of summer climate trigger thousands of thermokarst landslides in a High Arctic environment. *Nature Communications*, *10*(1), 1329. https://doi.org/10.1038/s41467-019-09314-7

Li, D., Li, Z., Zhou, Y., & Lu, X. (2020). Substantial increases in the water and sediment fluxes in the Headwater Region of the Tibetan Plateau in response to global warming. *Geophysical Research Letters*, *47*(11), e2020GL087745. https://doi.org/10.1029/2020GL087745

Li, D., Lu, X. X., Chen, L., & Wasson, R. J. (2019). Downstream geomorphic impact of the Three Gorges Dam: With special reference to the channel bars in the Middle Yangtze River. *Earth Surface Processes and Landforms*, *44*(13), 2660–2670. https://doi.org/10.1002/esp.4691

Li, D., Overeem, I., Kettner, A. J., Zhou, Y., & Lu, X. (2021a). Air temperature regulates erodible landscape, water, and sediment fluxes in the permafrost-dominated catchment on the Tibetan Plateau. *Water Resources Research*, *57*(2), e2020WR028193. https://doi.org/10.1029/2020WR028193

Li, D., Lu, X., Overeem, I., Walling, D., Syvitski, J., Kettner, A. J., et al. (2021b). Exceptional increases in fluvial sediment fluxes in a warmer and wetter High Mountain Asia. *Science*, abi9649. https://doi.org/10.1126/science.abi9649

Li, Z., Li, Z., Feng, Q., Zhang, B., Gui, J., Xue, J., & Gao, W. (2020). Runoff dominated by supra-permafrost water in the source region of the Yangtze river using environmental isotopes. *Journal of Hydrology*, *582*, 124506. https://doi.org/10.1016/j.jhydrol.2019.124506

Lian, X., Piao, S., Li, L. Z. X., Li, Y., Huntingford, C., Ciais, P., et al. (2020). Summer soil drying exacerbated by earlier spring greening of northern vegetation. *Science Advances*, *6*(1): eaax0255. https://doi.org/10.1126/sciadv.aax0255

Lloyd, C. E. M., Freer, J. E., Johnes, P. J., & Collins, A. L. (2016). Using hysteresis analysis of high-resolution water quality monitoring data, including uncertainty, to infer controls on nutrient and sediment transfer in catchments. *The Science of the Total Environment*, *543*(Pt A), 388–404. https://doi.org/10.1016/j.scitotenv.2015.11.028

Mather, A. L., & Johnson, R. L. (2014). Quantitative characterization of stream turbidity-discharge behavior using event loop shape modeling and power law parameter decorrelation. *Water Resources Research*, *50*(10), 7766–7779. https://doi.org/10.1002/2014wr015417

Misset, C., Recking, A., Legout, C., Poirel, A., Cazilhac, M., Esteves, M., & Bertrand, M. (2019). An attempt to link suspended load hysteresis patterns and sediment sources configuration in alpine catchments. *Journal of Hydrology*, *576*, 72–84. https://doi.org/10.1016/j.jhydrol.2019.06.039

Morehead, M. D., Syvitski, J. P., Hutton, E. W. H., & Peckham, S. D. (2003). Modeling the temporal variability in the flux of sediment from ungauged river basins. *Global and Planetary Change*, *39*(1–2), 95–110. https://doi.org/10.1016/s0921-8181(03)00019-5

Nash, J. E., & Sutcliffe, J. V. (1970). River flow forecasting through conceptual models part I—A discussion of principles. *Journal of Hydrology*, *10*(3), 282–290. https://doi.org/10.1016/0022-1694(70)90255-6

Nie, Y., Pritchard, H. D., Liu, Q., Hennig, T., Wang, W., Wang, X., et al. (2021). Glacial change and hydrological implications in the Himalaya and Karakoram. *Nature Reviews Earth & Environment*, *2*, 91–106. https://doi.org/10.1038/s43017-020-00124-w

Overeem, I., Hudson, B. D., Syvitski, J. P. M., Mikkelsen, A. B., Hasholt, B., van den Broeke, M. R., et al. (2017). Substantial export of suspended sediment to the global oceans from glacial erosion in Greenland. *Nature Geoscience*, *10*(11), 859–863. https://doi.org/10.1038/ngeo3046

Pietroń, J., Jarsjö, J., Romanchenko, A. O., & Chalov, S. R. (2015). Model analyses of the contribution of in-channel processes to sediment concentration hysteresis loops. *Journal of Hydrology*, *527*, 576–589. https://doi.org/10.1016/j.jhydrol.2015.05.009

Ranasinghe, R., Wu, C. S., Conallin, J., Duong, T. M., & Anthony, E. J. (2019). Disentangling the relative impacts of climate change and human activities on fluvial sediment supply to the coast by the world's large rivers: Pearl River Basin, China. *Scientific Reports*, *9*(1), 9236. https://doi.org/10.1038/s41598-019-45442-2

Rodzik, J., Furtak, T., & Zglobicki, W. (2009). The impact of snowmelt and heavy rainfall runoff on erosion rates in a gully system, Lublin Upland, Poland. *Earth Surface Processes and Landforms*, *34*(14), 1938–1950. https://doi.org/10.1002/esp.1882

Rowland, J. C., Jones, C. E., Altmann, G., Bryan, R., Crosby, B. T., Hinzman, L. D., et al. (2010). Arctic Landscapes in Transition: Responses to Thawing Permafrost. *Eos, Transactions American Geophysical Union*, *91*(26), 229–230. https://doi.org/10.1029/2010EO260001

Shi, R., Yang, H., & Yang, D. (2020). Spatiotemporal variations in frozen ground and their impacts on hydrological components in the source region of the Yangtze River. *Journal of Hydrology*, *590*, 125237. https://doi.org/10.1016/j.jhydrol.2020.125237

Simoni, A., Bernard, M., Berti, M., Boreggio, M., Lanzoni, S., Stancanelli, L. M., & Gregoretti, C. (2020). Runoff-generated debris flows: Observation of initiation conditions and erosion-deposition dynamics along the channel at Cancia (eastern Italian Alps). *Earth Surface Processes and Landforms*, *45*(14), 3556–3571. https://doi.org/10.1002/esp.4981

Smith, H. G., & Dragovich, D. (2009). Interpreting sediment delivery processes using suspended sediment-discharge hysteresis patterns from nested upland catchments, south-eastern Australia. *Hydrological Processes*, *23*(17), 2415–2426. https://doi.org/10.1002/hyp.7357

Syvitski, J. P., & Milliman, J. D. (2007). Geology, geography, and humans battle for dominance over the delivery of fluvial sediment to the coastal ocean. *The Journal of Geology*, *115*(1), 1–19. https://doi.org/10.1086/509246

Syvitski, J. P., Morehead, M. D., Bahr, D. B., & Mulder, T. (2000). Estimating fluvial sediment transport: The rating parameters. *Water Resources Research*, *36*(9), 2747–2760. https://doi.org/10.1029/2000WR900133

Syvitski, J. P. M. (2002). Sediment discharge variability in Arctic rivers: Implications for a warmer future. *Polar Research*, *21*(2), 323–330. https://doi.org/10.3402/polar.v21i2.6494

Taylor, R. J., Massey, C., Fuller, I. C., Marden, M., Archibald, G., & Ries, W. (2018). Quantifying sediment connectivity in an actively eroding gully complex, Waipaoa catchment, New Zealand. *Geomorphology*, *307*, 24–37. https://doi.org/10.1016/j.geomorph.2017.10.007

VanSickle, J., & Beschta, R. L. (1983). Supply-based models of suspended sediment transport in streams. *Water Resources Research*, *19*(3), 768–778. https://doi.org/10.1029/WR019i003p00768

Vercruysse, K., Grabowski, R. C., & Rickson, R. J. (2017). Suspended sediment transport dynamics in rivers: Multi-scale drivers of temporal variation. *Earth-Science Reviews*, *166*, 38–52. https://doi.org/10.1016/j.earscirev.2016.12.016

Vörösmarty, C. J., Meybeck, M., Fekete, B., Sharma, K., Green, P., & Syvitski, J. P. M. (2003). Anthropogenic sediment retention: Major global impact from registered river impoundments. *Global and Planetary Change*, *39*(1–2), 169–190. https://doi.org/10.1016/s0921-8181(03)00023-7

Walling, D., & Webb, B. (1982). *Sediment availability and the prediction of storm-period sediment yields* (p. 137). IAHS-AISH Publication

Wang, R., Yao, Z., Liu, Z., Wu, S., Jiang, L., & Wang, L. (2015). Snow cover variability and snowmelt in a high-altitude ungauged catchment. *Hydrological Processes*, *29*(17), 3665–3676. https://doi.org/10.1002/hyp.10472

Wang, T., Zhao, Y., Xu, C., Ciais, P., Liu, D., Yang, H., et al. (2021). Atmospheric dynamic constraints on Tibetan Plateau freshwater under Paris climate targets. *Nature Climate Change*, *11*(3), 219–225. https://doi.org/10.1038/s41558-020-00974-8

Williams, G. P. (1989). Sediment concentration versus water discharge during single hydrologic events in rivers. *Journal of Hydrology*, *111*(1), 89–106. https://doi.org/10.1016/0022-1694(89)90254-0

Wohl, E., Brierley, G., Cadol, D., Coulthard, T. J., Covino, T., Fryirs, K. A., et al. (2019). Connectivity as an emergent property of geomorphic systems. *Earth Surface Processes and Landforms*, *44*(1), 4–26. https://doi.org/10.1002/esp.4434

Wu, G. L., Liu, Y. F., Cui, Z., Liu, Y., Shi, Z. H., Yin, R., & Kardol, P. (2020). Trade-off between vegetation type, soil erosion control and surface water in global semi-arid regions: A meta-analysis. *Journal of Applied Ecology*, *57*(5), 875–885. https://doi.org/10.1111/1365-2664.13597

Wu, S., Yao, Z., Huang, H., Liu, Z., & Chen, Y. (2013). Glacier retreat and its effect on stream flow in the source region of the Yangtze River. *Journal of Geographical Sciences*, *23*(5), 849–859. https://doi.org/10.1007/s11442-013-1048-0

Yao, Z., Liu, Z., Huang, H., Liu, G., & Wu, S. (2014). Statistical estimation of the impacts of glaciers and climate change on river runoff in the headwaters of the Yangtze River. *Quaternary International*, *336*, 89–97. https://doi.org/10.1016/j.quaint.2013.04.026

Zheng, L., Overeem, I., Wang, K., & Clow, G. D. (2019). Changing Arctic River dynamics cause localized permafrost thaw. *Journal of Geophysical Research: Earth Surface*, *124*(9), 2324–2344. https://doi.org/10.1029/2019jf005060

Zong-Jie, L., Zong-Xing, L., Ling-Ling, S., Jin-Zhu, M., & Yong, S. (2018). Environment significance and hydrochemical characteristics of supra-permafrost water in the source region of the Yangtze River. *The Science of the Total Environment*, *644*, 1141–1151. https://doi.org/10.1016/j.scitotenv.2018.07.029